C/EBPβ regulates lipid metabolism and Pparg isoform 2 expression in alveolar macrophages

Dörr D., Obermayer B., Weiner J.M., Zimmermann K., Anania C., Wagner L.K., Lyras E.M., Sapozhnikova V., Lara-Astiaso D., Prósper F., Lang R., Lupiáñez D.G., Beule D., Höpken U.E., Leutz A., Mildner A.

Science Immunology
2022 SEP ; 7(75): eabj0140
2022 SEP 16 (first published online: final publication)
DOI: 10.1126/sciimmunol.abj0140

Publisher: American Association for the Advancement of Science (AAAS)

C/EBPβ regulates lipid metabolism and *Pparg* isoform 2 expression in alveolar macrophages

Dorothea Dörr[1,2], Benedikt Obermayer[3], January Mikolaj Weiner[3], Karin Zimmermann[1], Chiara Anania[4], Lisa Katharina Wagner[1], Ekaterini Maria Lyras[1], Valeriia Sapozhnikova[1], David Lara-Astiaso[5], Felipe Prósper[6,7], Roland Lang[8], Darío G. Lupiáñez[4], Dieter Beule[3], Uta E. Höpken[1], Achim Leutz[1,2] and Alexander Mildner[1,9,10]

[1] Max-Delbrück-Center for Molecular Medicine in the Helmholtz Association (MDC), Berlin, Germany.
[2] Institute of Biology, Humboldt University of Berlin, Berlin, Germany
[3] Core Unit Bioinformatics, Berlin Institute of Health, Charité - Universitätsmedizin Berlin, Berlin, Germany
[4] Max-Delbrück-Center for Molecular Medicine in the Helmholtz Association (MDC), Berlin Institute for Medical Systems Biology (BIMSB), Epigenetics and Sex Development Group, Berlin, Germany.
[5] Advanced Genomics Laboratory, Program of Hemato-Oncology, Center for Applied Medical Research (CIMA), University of Navarra, Pamplona, Spain.
[6] Program of Regenerative Medicine, Program of Hemato-Oncology, Center for Applied Medical Research (CIMA), University of Navarra, Pamplona, Spain.
[7] Instituto de Investigación Sanitaria de Navarra (IdiSNA), Pamplona, Spain
[8] Institute of Clinical Microbiology, Immunology and Hygiene, Universitätsklinikum Erlangen, Friedrich-Alexander-Universität Erlangen-Nürnberg, Erlangen, Germany
[9] Institute of Biomedicine, Medicity University of Turku, Turku, Finland
[10] InFLAMES Research Flagship Center, University of Turku, Turku, Finland
Correspondence: Alexander.Mildner@utu.fi (AM)

Abstract

Pulmonary alveolar proteinosis (PAP) is a syndrome characterized by accumulation of surfactant lipoproteins within the lung alveoli. Alveolar macrophages (AMs) are crucial for surfactant clearance, and their differentiation depends on colony-stimulating factor 2 (CSF2) and the establishment of an AM-characteristic gene regulatory network. Here we report that the transcription factor C/EBPβ is essential for the development of the AM identity, as demonstrated by transcriptome and chromatin accessibility analysis. Furthermore, C/EBPβ-deficient AMs showed severe defects in proliferation, phagocytosis, and lipid metabolism, collectively resulting in a PAP-like syndrome. Mechanistically, the long C/EBPβ protein variants LAP* and LAP together with CSF2 signaling induced expression of *Pparg* isoform 2, but not *Pparg* isoform 1, a molecular regulatory mechanism that was also observed in other CSF2-primed macrophages. These results uncover C/EBPβ as a key regulator of AM cell fate and shed light on the molecular networks controlling lipid metabolism in macrophages.

One sentence summary:

The molecular network of surfactant lipid metabolism in alveolar macrophages is orchestrated by the transcription factor C/EBPβ.

Introduction

Tissue-resident macrophages (TRMs) are immune sentinels, and also serve a critical function within tissues to maintain homeostasis. Development and specialization of these cells are adjusted to the physiological needs of their organ of residence. As such, alveolar macrophages (AMs), the resident macrophages in the lung alveoli, play an essential role in the maintenance of lung homeostasis, including the clearance of surfactant lipoproteins (*1*). Impaired degradation of surfactant lipoproteins by AMs results in the accumulation of excessive surfactant within the alveolar space and leads to the development of pulmonary alveolar proteinosis (PAP), a syndrome associated with impaired respiratory function and increased susceptibility to pulmonary infections (*2*).

AMs are locally self-maintaining cells that are established during embryogenesis and remain largely independent of circulating bone marrow (BM)-derived monocyte replenishment under physiological conditions (*3*). In mice, liver-derived fetal monocytes (F-Mo) start to colonize the lung around day 14 of embryonic development (E14). Once in the pulmonary tissue, F-Mo are exposed to environmental lung factors that direct their differentiation into immature AMs (pre-AMs), which begin to accumulate around E18 and subsequently give rise to mature AMs during the first postnatal days (*4*, *5*).

Colony-stimulating factor 2 (CSF2; also known as GM-CSF), which is produced by alveolar type II epithelial cells (*6*), is an indispensable growth factor involved in the differentiation of F-Mo and pre-AMs into mature AMs. Mice and humans that lack functional CSF2 signaling fail to develop AMs and, as a consequence, establish PAP syndrome (*2*). It was previously reported that in AMs, CSF2 signaling induces expression of the transcription factor (TF) peroxisome proliferator-activated receptor gamma (PPARγ), which subsequently directs the establishment of the AM-characteristic transcriptional identity and their tissue-specific function (*7*). Accordingly, adult *Pparg*-deficient animals only harbor non-classical AM-like cells that display phenotypical alterations, including defects in lipid metabolism and accumulation of surfactant lipoproteins, and develop a PAP-like phenotype (*7*).

The TF CCAAT-enhancer binding protein beta (C/EBPβ) is a regulator of adipocyte differentiation and of myeloid cell-mediated inflammatory processes, such as emergency granulopoiesis (*8*-*10*). Moreover, the development of a few myeloid populations, namely blood-resident Ly6C$^-$ monocytes and peritoneal macrophages (PMs), has been described to be C/EBPβ-dependent under homeostatic conditions (*11*, *12*). AM cell numbers were also reported to be affected by C/EBPβ-deficiency (*11*, *12*). However, the exact molecular function of C/EBPβ in AM biology and its potential regulatory interplay with other key AM factors remain unknown.

Here we unravel the function and molecular mechanisms of C/EBPβ in AMs. AMs from adult *Cebpb*-deficient mice showed impaired phagocytosis, a dysregulated lipid

metabolism and attenuated proliferation, collectively accumulating in a PAP-like pathology. Similar changes were detected in a transgenic mouse line that expresses only the truncated, short isoform of C/EBPβ, LIP. Furthermore, our data demonstrate that AMs, in contrast to other TRMs, expressed *Pparg* isoform 2 (*Pparg2*), while C/EBPβ-deficient AMs failed to induce specifically this *Pparg* isoform. We identified CSF2 signaling and C/EBPβ as necessary cofactors for the induction of *Pparg2* not only in AMs, but also in other *Cebpb*-expressing macrophages. These findings suggest a conserved regulatory machinery of lipid metabolism across distinct macrophage subsets. Our results further indicate a dichotomic regulation and function of the PPARγ1 and PPARγ2 isoforms.

Collectively, our data establish C/EBPβ as the missing regulatory link between CSF2 signaling and critical *Pparg2* isoform selection. Targeting the CSF2:C/EBPβ:PPARγ axis appears as a promising strategy to modulate macrophage-dependent lipid turnover not only in PAP but also in other lipid-associated diseases.

Results

C/EBPβ-deficiency leads to AM alterations and PAP-like pathology in mice

The TF C/EBPβ has been proposed to be involved in the regulation of AM development (*12*). However, the exact molecular functions of C/EBPβ and the related regulatory mechanisms in AM biology remain unknown. To investigate the role of C/EBPβ in AMs, we analyzed bronchoalveolar lavage fluid (BALF) and lung tissue of mice harboring a constitutive *Cebpb* gene deletion. Using flow cytometry, we found that adult *Cebpb* knock-out (KO) mice (7-16 weeks) showed reduced numbers of classical AMs (CD11b^{low} AMs; F4/80^{pos} CD11b^{lo} Siglec-F^{hi} CD11c^{hi}; Fig. 1A,B; gating strategy in fig. S1A,B). However, the lungs and BALF of KO mice additionally contained a population of AMs, which expressed the characteristic AM markers F4/80, Siglec-F and CD11c and displayed increased expression of the surface marker CD11b (CD11b^{high} AMs) (Fig. 1A-C).

Flow cytometry additionally revealed the presence of high amounts of debris in BALF from C/EBPβ-deficient mice (Fig. 1A). This finding was in line with an increased turbidity of BALF that was macroscopically visible and quantifiable by optical density measurement at a wavelength of 600nm (Fig. 1D). A specific enzyme-linked immunosorbent assay (ELISA) revealed elevated concentrations of surfactant protein D in BALF of C/EBPβ KO mice (Fig. 1E), which is indicative of PAP pathology. BALF cytospins in combination with May-Grünwald-Giemsa staining revealed that AMs from C/EBPβ$^{-/-}$ mice included numerous enlarged cells with a foamy cell-like morphology (Fig. 1F).

To investigate if C/EBPβ was required for the embryonic and perinatal development of AMs, we analyzed the lungs of C/EBPβ KO mice at prenatal stage E18 and postnatal day 3 (P3; gating strategy in fig. S1C-E). While the lungs of E18 wildtype (WT) and C/EBPβ KO embryos showed comparable numbers of F-Mo, C/EBPβ KO pre-AMs were reduced compared to WT littermates (Fig. 1G). At P3 most WT pre-AMs had developed into mature CD11c^{hi} Siglec-F^{hi} CD11b^{lo} AMs. C/EBPβ KO pups lacked these cells almost entirely, while a population of CD11c^{int} Siglec-F^{int} CD11b^{high} cells, reminiscent of immature AMs (*4*), was detected (Fig. 1H).

Taken together these findings show that prenatal AM development is C/EBPβ-dependent, and that C/EBPβ-deficiency leads to the development of a PAP-like phenotype in adult mice.

C/EBPβ directs AM identity and lipid metabolic processes

To investigate the role of C/EBPβ in AMs in more detail, we analyzed FACS-isolated lung Ly6C^{high} F-Mo and pre-AMs from WT and C/EBPβ KO E18 embryos and performed bulk RNA-sequencing (RNA-seq; n=3-4 per genotype; gating strategy in fig. S1C,D; Suppl. Data 1). Comparative analysis of E18 F-Mo revealed only 39 significantly differentially expressed genes (DEGs) between both genotypes (adj. p-value < 0.01 and |log2FC| > 2; Fig. 2A). In

contrast, pre-AMs from C/EBPβ KO mice showed 183 downregulated genes including *Pparg*, *Lpl* and *Abcd2*, while 332 genes were upregulated (e.g. *Etv3*, *Cd209a* and *Clec10a*; Fig. 2B) compared to WT controls. Gene ontology (GO) enrichment analysis revealed that upregulated genes in C/EBPβ KO pre-AMs were associated with processes such as antigen presentation, inflammatory response, and T cell activation, while downregulated genes were involved in foam cell differentiation, lipid storage and neutral lipid metabolic processes (Fig. 2C).

We next isolated AMs by FACS from BALF of adult WT mice, and both $CD11b^{low}$ and $CD11b^{high}$ AMs from C/EBPβ KO mice, and performed transcriptomic analysis. Comparison of the three populations revealed 1308 significant DEGs (adj. p-value < 0.01 and |log2FC| > 1 in at least one pairwise comparison; Fig. 2D and Suppl. Data 1). The DEGs could be divided into three clusters. Cluster 1 (264 genes) comprised genes with lowest expression in $CD11b^{high}$ KO AMs. Genes in cluster 2 (330 genes) were commonly downregulated in C/EBPβ KO AMs and cluster 3 (714 genes) contained upregulated genes in C/EBPβ KO AMs. Even though we detected transcriptomic differences between $CD11b^{low}$ and $CD11b^{high}$ KO AMs (mainly represented in cluster 1), principal component (PC) and correlation analysis revealed close similarity between both KO populations, while they were both clearly different from WT AMs (Fig. 2E). Of note, the absence of *Cebpb* did not result in a compensatory upregulation of other *Cebp*-family members nor did it negatively affect the surface expression of CSF2RA and CSF2RB (Fig. 2F; fig. S2A). In contrast, the characteristic AM signature according to a previously identified set of AM-specific genes (*13*) was diminished in C/EBPβ KO AMs (fig. S2B).

Next, we performed GO enrichment analysis of the identified DEGs. Cluster 1 revealed no biologically noteworthy results, while cluster 2 comprised genes linked to lipid metabolism pathways such as lipid catabolic process and fatty acid metabolic process, and included *Fabp1*, *Acox1*, *Olr1*, *Srebf2*, *Lsr* and the key AM and lipid metabolism regulator *Pparg* (Fig. 2F,G). Even though *Cidec* and *Agnptl* were included in cluster 1, both genes were significantly downregulated in both KO populations. Cluster 3 showed genes involved in antigen presentation including *Cd74* and *H2-Aa* and genes involved in the GO terms ‘innate immune response’, ‘negative regulation of cell proliferation’ and ‘chemotaxis’. Furthermore, genes required for lipid transport, such as *Abcb1a* and *Trem2,* were increased in KO AMs (Fig. 2F,G).

Differences in housing conditions, as well as sex-related gene changes, can affect the functions and transcriptomes of macrophages (*14*, *15*). To control for these secondary factors that might influence the phenotype of C/EBPβ KO AMs, we performed RNA-seq experiments of mice housed in different facilities, and of female and male C/EBPβ KO mice with their respective controls (fig. S2C-F). Housing- and sex-specific differences were indeed

detectable in C/EBPβ-deficient AMs, yet core transcriptomic changes, such as defects in immune response (upregulated in C/EBPβ KO AMs) and lipid metabolism (downregulated in C/EBPβ KO AMs), were inherent to *Cebpb*-deficient AMs irrespective of sex or housing conditions (fig. S2C-F).

Since we observed the downregulation of the key AM TF *Pparg* in *Cebpb*-deficient cells at the E18 pre-AM and adult stages, we explored the temporal sequence of *Cebpb* and *Pparg* expression in AMs. F-Mo was the earliest precursor stage investigated, and already expressed high levels of *Cebpb*, but the expression of *Pparg* only started to increase in Ly6C^{int} pre-AMs (Fig. 2H; gating strategy in fig. S1C,D), which is in line with a previous report (*5*). Notably, pre-AMs of *Cebpb*-deficient mice showed a strong reduction of *Pparg* transcripts (Fig. 2H). We furthermore analyzed the expression of genes involved in the KEGG PPAR signaling pathway (mmu03320) in *Cebpb*-deficient and WT E18 pre-AMs and adult AMs (Fig. 2I). Genes involved in the PPAR pathway were highly expressed in adult WT AMs and to a lesser extent also in their E18 precursors (Fig. 2I). The absence of C/EBPβ led to a deregulation of PPAR signaling-related genes in immature and adult *Cebpb*-deficient AMs (Fig. 2I).

Our transcriptomic data suggest a critical regulatory role of C/EBPβ in the lipid metabolism and immune function of immature and mature AMs.

C/EBPβ-deficient AMs are functionally impaired

The transcriptomic profile of adult CD11b^{low} and CD11b^{high} KO AMs indicated a functional impairment in their phagocytic and proliferative capacities. To corroborate this finding, we isolated AMs from C/EBPβ KO and WT littermates, incubated them with fluorescent beads and examined bead uptake by flow cytometry. In contrast to WT AMs, both CD11b^{low} and CD11b^{high} C/EBPβ KO AMs showed a compromised phagocytic activity (Fig. 3A). We then used the interferon (IFN) type I-inducible Mx-Cre system (*16*) to test if the phagocytic impairment of AMs was directly C/EBPβ-dependent or was due to a secondary effect of the observed PAP phenotype and the accumulation of lipids in C/EBPβ-deficient lungs (Fig. 1D). AMs from Mx-Cre *Cebpb*$^{fl/fl}$ and Mx-Cre *Cebpb*$^{+/+}$ mice were isolated and cultured with CSF2 (Fig. 3B). After 7 days, cells were treated with IFNα to induce Mx-Cre-mediated *Cebpb* deletion and were analyzed for phagocytic activity at day 14. As shown in Fig. 3C, Cre-induced deletion of *Cebpb* resulted in significantly reduced phagocytosis ($p < 0.001$).

We analyzed the proliferation capacity of C/EBPβ KO AMs. Isolated WT and C/EBPβ KO AMs were labeled with the fluorescent dye carboxyfluorescein succinimidyl ester (CFSE) and were cultured for up to 7 days *in vitro* in the presence of CSF2 to induce proliferation. The proportion of CFSE-negative cells was measured to detect proliferating cells. The fraction of CFSE-negative WT AMs increased from 0% (SD±0.1%) to 85% (SD±16.0%) by day 7, while

the CFSE-negative cell fraction in C/EBPβ KO only reached 25% (SD±25.5%; Fig. 3D), indicating an impaired capacity for proliferation. Of note, CD11b^{low} and CD11b^{high} KO AMs could not be discriminated in this assay since upregulation of CD11b expression was observed during *in vitro* culture of AMs. To investigate this point in more detail, we FACS-isolated WT and CD11b^{low} and CD11b^{high} C/EBPβ KO AMs, cultured them in the presence of CSF2 and tracked their cell numbers over the course of two weeks (Fig. 3E). We detected a steady increase of WT AMs, but both CD11b^{low} and CD11b^{high} C/EBPβ-deficient cells showed no change in cell numbers.

Finally, as our transcriptomic analysis indicated defects in lipid metabolism in C/EBPβ KO AMs, we compared the intracellular lipid storage of AMs from C/EBPβ-deficient and -proficient mice by Bodipy (Fig. 3F) and Oil Red O (Fig. 3G) staining. These assays revealed an accumulation of neutral lipids in both CD11b^{low} and CD11b^{high} mutant AMs.

Taken together these results demonstrate that the absence of C/EBPβ in AMs impairs their phagocytic and proliferative capacity in a cell-intrinsic manner and leads to a foamy macrophage phenotype.

Key functional AM programs require cell-intrinsic expression of C/EBPβ

The C/EBPβ-dependent transcriptomic changes of AMs could either be AM-intrinsic effects or involve indirect mechanisms via other cells. To distinguish between these possibilities, we analyzed adult CD11c-Cre *Cebpb*$^{fl/fl}$ and LyzM-Cre *Cebpb*$^{fl/fl}$ mice, in which *Cebpb* is deleted in CD11c^{+} cells or myeloid cells, respectively (*17*). Flow cytometric analysis revealed that CD11c-Cre *Cebpb*$^{fl/fl}$ mice had a similar phenotype to C/EBPβ KO mice with CD11b^{high} cells and reduced cell numbers of BAL CD11b^{low} AMs (fig. S3A,B). Furthermore, the turbidity of BALF from CD11c-Cre *Cebpb*$^{fl/fl}$ mice was significantly increased compared to littermate controls (fig. S3C; $p < 0.001$). Similar results were obtained for LyzM-Cre *Cebpb*$^{fl/fl}$ mice, which showed reduced AM cell numbers in BALF and lung tissue (fig. S3D-F). However, both conditional KO lines showed an overall lower frequency of CD11b^{high} AMs compared to C/EBPβ KO mice (Fig. 1A; fig. S3A,D). The increase in BALF turbidity in either of the two Cre *Cebpb*$^{fl/fl}$ lines was also less pronounced as in C/EBPβ KO mice, indicating a milder phenotype (Fig. 1D; fig. S3C,F).

Comparison of the transcriptomes of AMs from *Cebpb*$^{-/-}$, CD11c-Cre *Cebpb*$^{fl/fl}$ and LyzM-Cre *Cebpb*$^{fl/fl}$ mice and their respective controls by RNA-seq showed an overlap in the expression patterns between the different KO models. AMs from *Cebpb*$^{-/-}$ and LyzM-Cre *Cebpb*$^{fl/fl}$ mice clustered together in PC analysis (fig. S3G,H; Suppl. Data 2). We identified a cluster of genes that were upregulated in all KO strains including *Trem2*, *Cd74* and *Abcb1a* (cluster 6), and genes in cluster 4 comprising *Pparg*, *Cebpb*, *Cidec* and *Fabp1* were downregulated in all *Cebpb*-deficient AMs (fig. S3G-I). GO enrichment analysis revealed that cluster 6 was

enriched for genes involved in the GO terms chemotaxis, inflammatory response, and immune effector process, while downregulated genes in cluster 4 were enriched for lipid catabolic process, cell division, and sterol biosynthetic process (fig. S3J).

The transcriptional differences between the KO models, together with the potentially less severe PAP phenotype in the conditional mouse lines, may likely reflect the different promoter-dependent temporal onsets of *Cebpb* gene excision (*7*). *Cebpb* is highly expressed in pre-AMs and lung F-Mo and required for the development of AMs from at least E18 onwards (Fig. 1G, Fig. 2H). LyzM-Cre-mediated gene excision in AM precursor cells, however, only occurs around E18, and *CD11c*-Cre-mediated gene excision is induced even later with the upregulation of CD11c around postnatal day 1 (*7*). Therefore, early C/EBPβ-dependent AM development is still unhindered in both conditional mouse lines, which may result in phenotypic variations between the three analyzed *Cebpb* KO models.

Collectively, these data demonstrate that C/EBPβ cell-intrinsically determines the transcriptomic programs of key AM functions such as lipid metabolism and antigen presentation. Additional C/EBPβ-dependent effects in non-myeloid cells may further contribute to the phenotype observed in *Cebpb*$^{-/-}$ mice.

C/EBPβ is required for the adaptation of monocytes to the AM niche after irradiation

Under specific conditions, such as inflammation or following lethal irradiation with BM transplantation, monocytes are able to adapt to a vacant alveolar niche and differentiate into functional AMs (*3*, *18*). To examine whether C/EBPβ-deficient BM-derived cells can differentiate into AMs, we set up BM transplantation experiments, in which CD45.1/1 WT BM cells were mixed with CD45.2/2 CD11c-Cre *Cebpb*$^{fl/fl}$ BM cells in a 1:2 ratio and injected into lethally irradiated CD45.1/2 recipients (Fig. 4A). 5 weeks after BM transplantation, the ratio between CD45.2^{+} CD11c-Cre *Cebpb*$^{fl/fl}$ and CD45.1^{+} WT AMs in the lungs was similar to the ratio of reconstituted Ly6C^{high} monocytes in the blood, which is indicative of a functional recruitment of *Cebpb*-deficient BM-derived cells to the lungs (Fig. 4B,C). In agreement with the critical role of C/EBPβ in the development of monocytes (*11*), the Ly6C^{high} and, to a much higher extent, the CD11c^{+} Ly6C^{low} monocyte compartment, showed a lower ratio of CD11c-Cre *Cebpb*$^{fl/fl}$ to WT cells than lymphocytes (Fig. 4C). At 10 weeks post transplantation, CD45.2^{+} CD11c-Cre *Cebpb*$^{fl/fl}$ lung and BAL AMs accounted for only a small fraction of the AM pool (2% SD±2%) and were almost completely outcompeted by WT cells. The BALF turbidity at 5 weeks was increased in C/EBPβ mixed chimeras, during which time *Cebpb*-deficient AMs were still present in the lungs. At 10 weeks after transfer, the turbidity normalized to control levels (Fig. 4D).

To gain information about the transcriptomic programs that regulate monocyte-to-AM differentiation, we performed bulk RNA-seq analysis at both time points using FACS-purified

CD45.1$^+$ WT and CD45.2$^+$ CD11c-Cre *Cebpb*$^{fl/fl}$ lung AMs from the same recipient animals (n=3-4 per group; Fig. 4E-G). We detected 3499 genes that were differentially expressed in at least one pairwise comparison (adj. p-value < 0.01 and |log2FC| > 1) and could be assigned to 5 clusters (Fig. 4E-G). The expression of genes in cluster 1 increased from 5 to 10 weeks after transfer in CD45.1$^+$ WT AMs but was downregulated in *Cebpb*-deficient cells at both time points. This cluster contained genes involved in the GO terms fatty acid oxidation and lipid catabolic process, such as *Pparg*, *Cidec* and *Lsr* (Fig. 4G,H). Genes that were specific to C/EBPβ KO AMs, independent of the isolation time point, could be detected in cluster 2 and were enriched for chemotaxis and lymphocyte activation. Genes involved in innate immune response and antigen processing and presentation were generally downregulated from 5 weeks to 10 weeks in both genotypes, but were more highly expressed overall in C/EBPβ KO cells. The absence of C/EBPβ also affected genes related to cell division pathways at 10 weeks post transfer (cluster 5), which likely contributes to the competitive disadvantage of C/EBPβ KO cells. A more detailed analysis of the KEGG PPAR signaling pathway indicated that WT cells upregulated genes involved in PPAR signaling from 5 to 10 weeks, while C/EBPβ-deficient BM-derived AMs were not able to induce expression of this gene set, even though the PAP phenotype and BALF turbidity was rescued by WT cells at 10 weeks post transfer (Fig. 4D,I).

These data show that *Cebpb*-deficient BM-derived cells are not able to adapt to the lung environment after irradiation. These findings suggested that C/EBPβ is cell-intrinsically required for the establishment of the AM lipid metabolism machinery not only in embryo-derived but also in BM-derived AMs.

The long C/EBPβ isoforms LAP* and LAP are required for proper AM development

The single exon *Cebpb* gene can be translated into three different protein isoforms by differential usage of alternative start sites: liver-enriched activating protein* (LAP*), liver-enriched activating protein (LAP) and the short liver-enriched inhibiting protein (LIP). The isoforms differ by the presence of a complex N-terminal transactivation domain (LAP* and LAP) or its absence (LIP) (Fig. 5A), and have been shown to be able to fulfill diverse and sometimes opposing functions in various regulatory settings (*19*). Under physiological conditions, AMs express all three C/EBPβ protein variants (Fig. 5B). To dissect the roles of the three C/EBPβ isoforms in the regulation of AMs, we analyzed the *Cebpb* mutant LIP mouse line, generated by a LIP knock-in at the *Cebpb* locus and thus lacking the LAP* and LAP sequence and expressing only the truncated LIP isoform (Fig. 5C; (*20*)). BALF analysis of adult LIP (*Cebpb*$^{LIP/LIP}$) mice by flow cytometry revealed phenotypic similarities to C/EBPβ KO mice, including the presence of CD11b^{high} AMs, although at lower frequency (Fig. 5D,E; Fig. 1A,B). In contrast to C/EBPβ KO mice, the number of CD11b^{low} AMs was not reduced in

LIP mice (Fig. 5D,E). Nevertheless, BALF turbidity was increased in these animals, indicating a functional impairment of AMs similar to C/EBPβ KO mice (Fig. 5F).

To compare AMs from C/EBPβ KO and LIP mice in more detail, we isolated AMs from LIP mice and WT control littermates (n=3-4 per genotype) and compared their transcriptomic profiles with those of C/EBPβ-deficient AMs. By pairwise comparisons of all analyzed populations, we detected 2684 DEGs (adj. p-value < 0.01 and |log2FC| > 1) that were grouped in 7 clusters (Fig. 5G; Suppl. Data 3). A large proportion of genes showed similar effects in LIP and KO AMs including the downregulation of genes involved in the GO terms 'fatty acid oxidation' and 'lipid catabolic process' (cluster 6), such as *Cidec*, *Fabp1* and *Pparg*, and the upregulation of genes related to MHCII antigen presentation, such as *Cd74* and *H2-Aa* (cluster 5; Fig. 5G-J). On the other hand, clusters 1 and 3 contained genes with an altered expression profile in KO but not in LIP AMs. Upregulated genes specific to KO AMs (cluster 3) included genes related to antigen processing via MHCI and ion homeostasis, while cluster 1 with genes downregulated specifically in KO AMs was characterized by the GO terms cholesterol biosynthetic process and steroid metabolic process (Fig. 5J). Genes in clusters 2 and 7 that were differentially expressed between the KO and the LIP mouse strain showed no specific gene enrichment and could be attributed to the different genetic backgrounds of the two mouse lines (Fig. 5G-J).

The common downregulation of genes involved in fatty acid oxidation and lipid catabolic process was also apparent from a markedly disturbed expression of the KEGG PPAR pathway in both C/EBPβ mutant strains (Fig. 5K). In contrast, the expression of sterol biosynthetic process-related genes was partly rescued by LIP expression *in vivo* (Fig. 5L). To validate these findings, we compared the composition of storage and membrane lipids in WT and mutant AMs by lipidomic analysis using Orbitrap mass spectrometry. $1x10^5$ FACS-isolated AMs from KO (n=3), LIP (n=4) ($CD11b^{low}$ and $CD11b^{high}$ AMs were pooled for both genotypes) and WT controls (n=3) were subjected to the analysis. Both KO and LIP AMs showed an approximately 3-fold higher lipid content compared to WT cells (Fig. 5M). Importantly, the major components of surfactant, namely phosphatidylcholine, phosphatidylethanolamine and phosphatidylglycerol, accumulated in both KO and LIP AMs. In line with the RNA-seq data, cholesterol esters were also enriched in *Cebpb*-deficient AMs, while their physiological concentrations were restored by LIP expression (Fig. 5N).

Together these data show that expression of the truncated C/EBPβ isoform LIP is not sufficient to overcome the C/EBPβ-dependent establishment of a PAP-like phenotype. However, LIP expression was found to rescue some of the C/EBPβ-deficiency-mediated transcriptional changes in AMs, especially those related to sterol and cholesterol biosynthetic processes.

DNA regions with RXRA:PPARγ motifs are less accessible in C/EBPβ-deficient AMs

To identify C/EBPβ-dependent DNA regions and uncover TFs that might cooperate with C/EBPβ and play a role in the observed AM phenotypes, we isolated BAL AMs and performed C/EBPβ ChIPmentation *(21)*. In comparison to input DNA control samples, C/EBPβ binding was detected at 18694 DNA regions, which could be assigned to 7604 nearest genes (Fig. 6A). Most of the C/EBPβ binding events were located in close proximity to transcriptional start sites (TSS) of genes (Fig. 6A). A comparison of the identified down- and upregulated genes in *Cebpb*-deficient AMs by RNA-seq (Fig. 2D) with the 7604 genes that showed C/EBPβ binding revealed that 58% of the upregulated genes ($p = 1.1x10^{-8}$) and 77% of the downregulated genes ($p = 2.2x10^{-16}$) showed at least one binding event of C/EBPβ (Fig. 6B; Suppl. Data 4). These data indicate that C/EBPβ can function as a repressor or activator of gene expression. TF motifs that were present in DNA sequences within C/EBPβ binding peaks showed a significant enrichment of C/EBP and PU.1 motifs (Fig. 6C; p < 1e-1000 and p < 1e-600 respectively). Motifs belonging to Etv2, JunB, KLF and IRF TFs, as well as PPAR motifs, were also evident in C/EBPβ binding sequences. GO enrichment analysis with all C/EBPβ-bound genes revealed that this set of genes was enriched for genes involved in immune system process, myeloid cell differentiation, phagocytosis, and lipid catabolic processes (Fig. 6D,E; fig. S4A).

To elaborate these findings in more detail we performed chromatin accessibility analysis by transposase-accessible chromatin-sequencing (ATAC-seq: *(22)*) of FACS-isolated AMs from WT, *Cebpb*-deficient (n=3 per genotype) and LIP knockin animals (n=4 per genotype). In total, 16186 differential peaks were detected in KO cells with $|log2FC| > 2$ and adj. p-value < 0.05 of which 5309 peaks (assigned to 2435 genes) indicated enhanced accessibility and 10877 peaks (assigned to 4054 genes) were less accessible in KO AMs (Fig. 6F and Suppl. Data 5). The changes in LIP AMs were less pronounced compared to KO cells and we detected 3130 peaks (assigned to 1421 genes) with a higher accessibility and 1348 peaks (assigned to 601 genes) that were less accessible in AMs isolated from LIP mice compared to littermates (Fig. 6F; Suppl. Data 6).

Next, we determined motif enrichment within the DNA regions corresponding to the differential peaks. Regions that were more accessible in KO and LIP AMs compared to WT cells were enriched for FOS and JUN motifs (Fig. 6G). *Cebpb*-deficiency also led to more open chromatin regions with IRF, RELA and NFkB motifs, which is in agreement with the C/EBPβ ChIPmentation data. Peaks with decreased accessibility in both KO and LIP AMs, were enriched for C/EBP and, importantly, RARA/RXRA/Rxra:Pparg motifs. The RNA expression levels of the identified TFs are depicted in fig. S4B. Similar results were obtained when we focused our analysis only on peaks in proximal TSS regions (±3kb from TSS) instead of all detected peaks (fig. S4C-E). When we compared the chromatin accessibility

with the transcriptomic signature of the same samples, we observed many concordant changes (Fig. 6H). An increase of chromatin accessibility was in general accompanied by an increase in RNA expression of the corresponding gene and *vice versa*. However, a fraction of genes showed a discordant behavior as described earlier (*23*). We identified genes like *Pparg,* which showed ATAC-seq rescue by LIP that was not accompanied by transcriptomic rescue, indicating the requirement of the C/EBPβ transactivation domain for induction of gene expression (Fig. 6I). Some genes, including *Acaa1a,* showed no ATAC-seq peak changes in *Cebpb* mutant cells compared to WT but had lower RNA expression. Moreover, the defects in *Nfatc2* could neither be rescued on chromatin nor RNA level by LIP expression. In summary, these data reveal that PPARγ motifs are present within many C/EBPβ binding regions, and that RXRA:PPARγ motifs in particular were less accessible in the absence of C/EBPβ.

Cebpb- and _Pparg_-deficient AMs share transcriptomic alterations

Our molecular analyses suggested an involvement of C/EBPβ in the regulation of PPARγ signaling in AMs. To further investigate this hypothesis, we compared the expression profiles of *Cebpb*-deficient AMs with published microarray data of AMs isolated from CD11c-Cre *Pparg*$^{fl/fl}$ mice that also develop PAP pathology (GSE60249; (*7*)). Many of the DEGs (adj. p-value < 0.01, |log2FC| > 1) between AMs isolated from CD11c-Cre *Pparg*$^{fl/fl}$ animals and WT controls overlapped with those detected in both C/EBPβ KO populations compared to WT cells. Especially CD11b^{high} KO AMs clustered together with *Pparg*-deficient AMs in PC analysis (fig. S5A-C). Many genes downregulated in both C/EBPβ- and PPARγ-deficient AMs were genes involved in lipid metabolism, including *Fabp1*, *Lsr* and *Cidec* (cluster 1; fig. S5A,C). However, also groups of PPARγ KO-specific and C/EBPβ KO-specific genes were detected. Thus, the data indicate an involvement of C/EBPβ in *Pparg* signaling.

C/EBPβ-mediated induction of _Pparg2_ requires CSF2

Our analysis revealed that the phenotype of C/EBPβ-deficient AMs shared some resemblance with the phenotype observed in PPARγ$^{-/-}$ AMs. *Pparg* transcripts exist in two isoforms: Isoform 1 (*Pparg1*) is expressed across many cell types, whereas expression of isoform 2 is more restricted, and especially reported for adipocytes (*24*). Another study demonstrated expression of PPARγ2 also in AMs (*25*). Since C/EBPβ is involved in the regulation of *Pparg2* during adipogenesis (*26*), we speculated that a similar mechanism might exist in AMs. Accordingly, we determined the expression of *Pparg1* and *Pparg2* in different TRM populations isolated from WT and *Cebpb*$^{-/-}$ animals by real-time PCR (Fig. 7A; gating strategies in fig. S1F-I). We detected *Pparg1* transcripts in all investigated TRM subsets (Fig. 7A). In contrast, *Pparg2* expression was essentially restricted to AMs and only

at low level observed in white adipose tissue macrophages (WAM). Absence of C/EBPβ led to strongly reduced expression of *Pparg2* in AMs (32-fold decrease in KO), indicating that C/EBPβ is specifically involved in *Pparg2* regulation. Similar results were observed in AMs isolated from LIP animals (Fig. 7B), from CD11c-Cre *Cebpb* flox mice (Fig. 7C) and from BM-derived AMs 10 weeks after transplantation (Fig. 7D).

To examine whether C/EBPβ plays a pioneering or a constitutive role in *Pparg2* expression, we again took advantage of the IFN type I-inducible Mx-Cre system (*16*) as described earlier (Fig. 3B). *Cebpb* expression was detected in Mx-Cre *Cebpb*$^{fl/fl}$ AMs before IFNα treatment at day 7 but was lost after IFNα treatment at day 14 (Fig. 7E). At the same time, *Pparg2* expression significantly decreased in IFNα-treated Mx-Cre *Cebpb*$^{fl/fl}$ cells, indicating that C/EBPβ is essential to maintain *Pparg2* expression in AMs. We used the same experimental set up to investigate the effect of IFNα-induced C/EBPβ deletion on the *Pparg* chromatin status. After 7 days in culture, AMs from Mx-Cre *Cebpb*$^{fl/fl}$ (n=3) and Mx-Cre *Cebpb*$^{+/+}$ (n=2) mice were treated with IFNα and harvested for ATAC-seq analysis at day 14. Loss of C/EBPβ in IFNα-treated Mx-Cre *Cebpb*$^{fl/fl}$ AMs led to a significantly decreased accessibility of the *Pparg2* locus, while other regions of the *Pparg* gene were not affected. Importantly, the affected regions also showed strong C/EBPβ binding in our ChIPmentation data (Fig. 7F).

To confirm the regulatory sequences responsible for the C/EBPβ-mediated induction of *Pparg2* expression, we cloned the *Pparg1* and *Pparg2* promoter regions, as well as a *Pparg2* enhancer element, which showed C/EBPβ binding in WT AMs (Fig. 7F-G), into a luciferase reporter vector. We transfected *Cebpb*-deficient mouse embryonic fibroblasts (MEFs) with the different promoter/enhancer constructs and introduced empty vector (con) or plasmids encoding one of the three C/EBPβ isoforms, LIP, LAP or LAP*. Measurement of the relative luciferase expression normalized to renilla luciferase activity revealed that the *Pparg1* promoter was active independent of C/EBPβ isoforms, while the *Pparg2* promoter responded to the long C/EBPβ isoforms LAP and LAP*, but not to LIP (Fig. 7H). The *Pparg2* enhancer element, however, was even more responsive to the long C/EBPβ isoforms and was sufficient to activate luciferase expression.

Expression of *Pparg* in AMs was shown to be induced by CSF2, however it was not discriminated between the different *Pparg* isoforms (*7*). Therefore we next tested if CSF2 is obligatory for *Pparg2* and *Cebpb* expression. We isolated WT AMs by BAL and cultured them either with CSF1 or CSF2 for 48h. Analysis by qPCR revealed that the expression of *Pparg2* was increased when AMs were treated with CSF2 as compared to cells cultured with CSF1 (85-fold SD±9.4), while *Cebpb* expression was unchanged (Fig. 7I). In line with this, inhibition of JAK1 and JAK2, an established transducer of CSF2 signaling (*27*), by Ruxolitinib prevented the CSF2-mediated induction of *Pparg2* but had only moderate effects on the expression of *Cebpb* (fig. S6A). These data indicate that CSF2 is mandatory for the

continuous maintenance of *Pparg2* but not of *Cebpb* transcripts in AMs. To verify this finding *in vivo*, we analyzed the transcriptomic profiles of FACS-purified pre-AMs from *Csf2rb*-deficient E18 embryos and compared them to *Cebpb*-deficient pre-AMs (fig. S6B-F; Suppl. Data 7; gating strategy in fig. S1C,D). Even though both genotypes showed differences in *Pparg* expression and genes involved in lipid signaling, *Cebpb* itself was similarly expressed in WT and *Csf2rb*-deficient pre-AMs (fig. S6E). These data again demonstrate that CSF2 does not induce *Pparg2* by regulating *Cebpb* mRNA levels.

Pparg isoform expression analysis revealed the absence of *Pparg2* in PMs and other TRM populations (Fig. 7A). To test if CSF2 can induce *Pparg2* also in these macrophage populations, we cultured PMs, which express high levels of *Cebpb* (Fig. 7A; immgen.org), with CSF1 or CSF2 for 48h. Treatment with CSF2 was able to induce *Pparg2* in PMs, while this isoform was barely detectable in CSF1-treated cells (83-fold SD±18.7 higher in CSF2-cultured cells; Fig. 7J). To investigate if C/EBPβ is also involved in this CSF2-dependent induction of *Pparg2* in PMs, we isolated PMs from WT, C/EBPβ KO and LIP mice by FACS and stimulated the cells with CSF2 for 48h. *Pparg2* expression was strongly diminished in *Cebpb*-deficient and LIP PMs (Fig. 7K; fig. S7A). Similar results were obtained for CSF2-cultured BM cells generated from C/EBPβ KO (Fig. 7K), CD11c-Cre *Cebpb* flox and LIP mice (fig. S7B-C).

Collectively our data show that the long C/EBPβ isoforms LAP and LAP* can directly induce the expression of *Pparg2* in the presence of active CSF2 signaling.

Discussion

Here we unravel the gene regulatory networks that are required for AM development and lipid metabolism, and thus for lung integrity, and identify C/EBPβ as a central player. We expand on previous studies that reported reduced AM cell numbers in C/EBPβ$^{-/-}$ mice (*12*) and show that the AM cell-intrinsic effects of C/EBPβ deletion result in a functionally compromised AM pool with defects in proliferation, phagocytosis and lipid metabolism, collectively resulting in PAP-like syndrome.

The development and maintenance of AMs relies on the bioavailability of CSF2 (*2*). The strong dependency of AMs on CSF2 is probably unique within the macrophage compartment, since most other TRM populations except for intestinal macrophages *(28)* are largely unaffected by genetic deletion of *Csf2* or *Csf2rb* under physiological conditions *(29, 30)*. One of the reasons why CSF2 might be evolutionarily selected for its function on lung AMs is that CSF2-signaling induces the nuclear receptor *Pparg* (*7*). In adipocytes, PPARγ controls the expression of genetic networks involved in lipid metabolism, transport and storage *(31)*. The presence of high lipoprotein concentrations in form of lung surfactant makes it plausible that similar functions of PPARγ are cell-intrinsically required in AMs to transport and metabolize ingested surfactant lipids. However, it is unlikely that CSF2-signaling induces *Pparg* expression without the cooperation of additional signals or TFs. During *in vitro* differentiation of pre-adipocytes, adipogenesis-supporting factors like 3-isobutyl-1-methylxanthine (IBMX) or dexamethasone (DEX) induce *Cebpb* expression *(32)*, which in cooperation with the glucocortoid receptor activates the expression of *Pparg2 (33)*. As a functional consequence, *Cebpb*-deficient mice show deficits in adipogenesis *in vivo (34)*. Of note, *Pparg2* is sufficient to further drive adipogenesis *in vitro*, while *Pparg1* is not *(35)*. In line with these data, we found that *Cebpb*-deficient AMs showed strongly reduced levels of *Pparg2*. Moreover, AMs lost expression and chromatin accessibility of *Pparg2* following MxCre-mediated deletion of *Cebpb in vitro*, indicating a continuous role of C/EBPβ for *Pparg2* induction. Similar to the situation in adipocytes *(36)*, the C/EBPβ isoforms LAP* and LAP, but not LIP, were able to interact with *Pparg2* promoter and enhancer elements, while *Pparg1* was inhibited by all C/EBPβ protein variants. In line with recent results reported for human monocyte-derived cells *(37)*, expression of *Pparg2* was also induced in WT, but not in *Cebpb*-deficient PMs or BM-derived monocytes cultured with CSF2. Interestingly, all three macrophage subsets are characterized by an open chromatin structure at the *Pparg2* promoter region *(38, 39)*. C/EBPβ binding at these positions was described for adipocytes *(40)*, CSF2-cultured BM-derived macrophages *(39)* and also AMs as shown here, which indicates that C/EBPβ is important for the accessibility of the *Pparg2* locus. LIP animals likewise showed an accessible *Pparg2* promoter but failed to induce its gene expression. Since LIP lacks the C/EBPβ transactivation domain, but includes the DNA-binding basic leucine zipper, the sole

chromatin accessibility seems to be insufficient for *Pparg2* induction. However, our data also show that LIP was able to rescue some of the defects observed in C/EBPβ-deficient AMs, which is in agreement with a recent report showing that many functions of LIP are not only dominant-negative in nature *(41)*.

It was previously shown that C/EBPβ requires post-translational phosphorylation to become an activator of adipogenesis *(36)*. Since PMs express high levels of *Cebpb* and show an accessible *Pparg2* locus, but do not normally transcribe this specific isoform, it is possible that CSF2 signaling induces post-translational modifications of C/EBPβ in macrophages that enable its function as an activator of *Pparg2*.

In macrophages, PPARγ was shown to be involved in anti-inflammatory processes during their inflammatory response *(42, 43)*. However, these studies did not distinguish between PPARγ1 and PPARγ2 isoforms. While *Pparg1* is expressed more widely among different TRM populations, we show here that expression of *Pparg2* appears to be specific to TRM populations with high exposure to CSF2 and/or a lipid-rich environment like AMs. This might reflect different properties of PPARγ1 and PPARγ2 in macrophage biology. In line with this notion, Vav-Cre *Pparg*$^{fl/fl}$ mice – in contrast to C/EBPβ KO mice – lack classical CD11b^{low} AMs almost completely (*7*), which might suggest that the expression of *Pparg1* in C/EBPβ KO AMs is sufficient to overcome some of the early functional defects observed in complete *Pparg*-deficient AMs.

Since our study mainly focused on C/EBPβ and its molecular actions, our data cannot fully dissect the functional differences between the two PPARγ isoforms. *Pparg* isoform-specific knock-out mice and isoform rescue experiments will be required to clarify the multifaceted roles of PPARγ in more detail. Another open question concerns the cellular origin of CD11b^{high} C/EBPβ KO AMs. Studies suggest origin-dependent differences in the molecular and functional properties of embryo- and monocyte-derived TRMs after experimentally induced niche liberation *(23, 44)*. Even though our experiments do not identify the ontogeny of CD11b^{high} C/EBPβ KO AMs, our data show lipid metabolism defects in *Cebpb*-deficient AM precursor cells, adult AMs, and monocyte-derived AMs. This argues for a dominant role of C/EBPβ in the establishment and regulation of AM lipid metabolism and identity independent of the cellular origin.

In summary, our data suggest C/EBPβ as a central player in PAP pathogenesis due to its function in macrophage lipid metabolism. The molecular mechanism of C/EBPβ-induced *Pparg2* expression may also be relevant for other pathologies where macrophages encounter high lipid concentrations and have to cope with lipid accumulation such as obesity or atherosclerosis.

Study design

The objective of this study was to investigate the functional and molecular role of C/EBPβ in AMs. We used different mutant *Cebpb* mouse models to isolate AMs at different developmental stages and examine the molecular and functional effects of C/EBPβ-deficiency or specific C/EBPβ isoform expression on AMs. We used flow cytometry, transcriptomic analysis by RNA-seq and qPCR, epigenetic analysis by ATAC-seq and ChIP-seq, lipidomics analysis and functional assays. Numbers of sampling and experimental replicates are indicated in the figure legends. Sample sizes were chosen according to previous comparable studies conducted in our laboratory and animal availability. Adult mice in control and test groups were age-, background- and sex-matched. For cell quantifications and *in vitro* cell cultures both male and female mice were used with no statistical differences between the sexes. Investigators were not blinded. Outliers were only excluded in bulk RNA-seq analyses based on poor sample quality.

Materials and Methods

Mice

The following mouse strains were used in this study: B6.Cg.129P2-C/EBPb tm1Pfj (*Cebpb*$^{-/-}$ mice; *(45)*), B6.Cg.129P2-C/EBPtm1.2Acle (LIP mice; (*20*)), B6.129P2-Lyz2tm1(cre)Ifo/J (LyzM-Cre mice; *(46)*); B6.SJL-Ptprca-Pepcb/BoyJ (CD45.1/1 mice); C57BL/6J-Tg(Itgax-cre,-EGFP)4097Ach/J (CD11c-Cre mice; *(47)*); B6.Cg-Tg(Mx1-cre)1Cgn/J (Mx-Cre mice; (*16*)), B6.129S1-Csf2rbtm1Cgb/J (*Csf2rb*$^{-/-}$ mice; *(29)*). BALB/cJ-Cebpbtm1.1Elgaz/J (*Cebpb*$^{fl/fl}$ mice; *(48)*) backcrossed to C57BL/6 were crossed with the respective Cre lines. The C/EBPβ$^{-/-}$ and LIP mice were kept on a mixed genetic background since these strains are not viable on a C57BL/6 background. Animals between 7 and 16 weeks of age were used for analysis, if not stated otherwise. For the generation of BM chimeras, 8-12 weeks old recipient mice (CD45.1/2) were lethally irradiated (950 rad). On the following day, the recipients were reconstituted with 5x10^6 BM cells, which were a mixture of 33% WT (CD45.1/1) and 66% CD11c-Cre *Cebpb*$^{fl/fl}$ (CD45.2/2; CD11c^{KO}) BM cells, by tail vein injection. The animals received an antibiotic treatment with Enrofloxacin in their drinking water for 10 days after irradiation. BM chimeras were analyzed 5 and 10 weeks after transfer. All mice were maintained in a special pathogen-free (SPF), temperature-controlled (22±1°C) mouse facility on a 12-h light, 12-h dark cycle at the Max-Delbrück Center, Berlin, Germany. Both here tested facilities (fig. S2C-E) were of FELASA SPF standard. However, in facility 1 *Helicobacter spp*., *Rodentibacter spp*. and Noroviruses were occasionally evident. Food and water were given *ad libitum*. Mice were fed a usual chow diet. All animal experiments have been approved by the LAGeSo in Berlin in accordance with international guidelines.

Cell isolation and preparation

Adult mice were killed by CO_2 inhalation or intraperitoneal injection of 150mg/kg body weight pentobarbital sodium (WDT). BALF was isolated by intratracheal instillation and withdrawal of five times 1ml PBS with 2mM EDTA and 1% heat-inactivated fetal bovine serum (FBS; Gibco) if not indicated otherwise. The fluid was filtered through a 100µm mesh and AMs were harvested by centrifugation. PMs were isolated by peritoneal lavage with PBS containing 2mM EDTA and 1% heat-inactivated FBS (Gibco). For the isolation of other TRMs mice were intracardially perfused with PBS before spleen, kidney and visceral white adipose tissue were removed. The spleen was dissociated through a 100µm cell strainer, red blood cells were lysed with ACK, the samples washed and then used for staining. Kidney and white adipose tissue were minced and digested with 1mg/ml collagenase type IV (Gibco) and 2mg/ml DNase I (Roche) in RPMI medium at 37°C for 30min while shaking. Following digestion, the samples were homogenized through a 100µm cell strainer, washed and white adipose tissue samples were stained. Kidney cell suspensions were subjected to density centrifugation with 40% Percoll (Sigma) at 700xg, 14°C for 20min with low acceleration and no brake before they were again washed and stained. For the isolation of BM cells, femur and tibia were removed and flushed with PBS containing 2mM EDTA and 1% heat-inactivated FBS (Gibco). Samples were then subjected to red blood cell lysis before further processing.

E18 embryos from time-mated mice were sacrificed by decapitation before their lungs were removed, minced and digested with 1mg/ml collagenase type IV (Gibco) and 2mg/ml DNase I (Roche) in RPMI medium at 37°C for 30min while shaking. After digestion the samples were filtered through a 100µm mesh, washed and stained.

Flow cytometry and cell sorting

All cells were blocked with anti-CD16/32 (2.4G2) before staining and antibodies against CD11b (M1/70), CD11c (N418), Siglec-F (E50-2440), F4/80 (BM8), CD64 (X54-5/7.1), CD115 (AFS98), Ly6C (HK1.4), Ly6G (1A8), CD3e (145-2c11), CD45 (30-F11), B220 (RA3-6B2), MHCII (IAb; AF6-102.1), Cx3cr1 (SA011F11), Ter119, CD131 (JORO50), CSF2RA (698423) and NK1.1 (PK136) from BioLegend, eBioscience and R&D Systems were used. Samples were flow-sorted using AriaI, AriaII or AriaIII (BD Biosciences, BD Diva Software) cell sorters. Flow cytometry analyses were performed on Fortessa or LSRII (BD Biosciences, BD Diva Software) and analyzed with FlowJo software v.10.7.1 (BD).

Turbidity quantification of BALF

For turbidity quantification of BALF 250µl out of 5ml BALF were diluted with 250µl PBS and the optical density measured at a wavelength of 600nm.

639

640 ELISA of surfactant protein D (SP-D)

641 BAL was performed using 1ml of PBS and spun down at 100xg for 3min to separate the fluid
642 supernatant from the cells. Subsequently supernatant of *Cebpb* KO samples was diluted
643 1:2500 and WT samples 1:1000 in PBS. The ELISA was performed using a Systems
644 Quantikine ELISA Kit for Mouse SP-D (R&D) according to the manufacturer's protocol.

645

646 May-Grünwald-Giemsa and Oil Red O staining

647 AMs were isolated by BAL and subjected to a Ficoll centrifugation to remove debris and dead
648 cells. Cytospins were performed at 500rpm with low acceleration for 5min. For May-
649 Grünwald-Giemsa stainings cytospins were fixed in methanol for 5min and stained with May-
650 Grünwald solution for 5min. Subsequently the samples were washed with water and stained
651 with a 5% Giemsa solution for 45min before they were again washed with water. For Oil Red
652 O stainings cytospins were fixed in 4% paraformaldehyde for 15min, washed with PBS,
653 rinsed with 60% isopropanol and then stained in a 0,3% Oil Red O (Sigma-Aldrich) solution
654 in 60% isopropanol for 60min. The slides were again rinsed with 60% isopropanol, stained
655 with heamatoxylin (AppliChem) for 50sec and washed with water.

656

657 Phagocytosis assay

658 AMs were isolated by BAL and seeded in RPMI complete medium (RPMI1640 GlutaMAX
659 supplemented with 10% FBS (Gibco), 1% sodium pyruvate (Gibco) and 1% penicillin-
660 streptomycin (Gibco)) in a non-tissue culture treated 6-well plate. The cells were incubated at
661 37°C for 2h to allow them to adhere. Next the cells were incubated with or without
662 fluorescent latex beads (Sigma-Aldrich) for 90min either at 37°C or on ice. Afterwards they
663 were washed with PBS three times, detached with trypsin, stained with surface marker
664 antibodies and analyzed by flow cytometry. To correct for unspecific adherence of the beads
665 to the outside of the cells, the median fluorescence intensity (MFI) of bead-positive cells was
666 calculated as follows: MFI of bead-positive cells incubated at 37°C – MFI of bead-positive
667 cells incubated on ice.

668

669 CFSE *in vitro* cell proliferation assay

670 AMs were isolated by BAL, resuspended in PBS with 5µM CFSE (BioLegend) and incubated
671 at 37°C for 20min to label the cells. Following incubation, the staining was quenched by
672 adding five times the staining volume of RPMI complete medium. The cells were pelleted and
673 seeded in RPMI medium in non-tissue culture treated 6-well plates. AMs were then
674 incubated at 37°C for 4h to allow them to adhere before non-adherent cells were removed
675 and the medium replaced by RPMI complete with 20ng/ml CSF2 (Stemcell Technologies).

AMs were cultured for up to 7 days and every 2 to 3 days the medium was replaced. On day 1, 4 and 7 fractions of the cells were harvested by trypsinization, stained with surface marker antibodies and analyzed by flow cytometry.

Bodipy staining

Freshly BAL-isolated AMs were stained with surface marker antibodies for flow cytometry before half of each sample was incubated in a 1:500 Bodipy 493/503 (Thermo Fisher Scientific) dilution in PBS at 37°C for 15min. The other half of each sample was resuspended in a 1:500 dilution of DMSO in PBS as controls. All samples were washed with PBS three times and analyzed by flow cytometry.

Basic lipidomic analysis

For lipidomic analysis $1x10^5$ AMs were sorted from BALF and frozen in liquid nitrogen. Quantitative analysis of lipids was performed by Lipotype GmbH, Dresden (www.lipotype.com) according to their standard “Basic lipidomics analysis” procedure using the Lipotype Shotgun Lipidomics technology together with high-resolution Orbitrap mass spectrometry.

RNA isolation and cDNA synthesis for RNA-seq and quantitative real-time PCR

Cells (500-20,000 sorted cells for RNA-seq) were lysed with 50-200µl of lysis/binding buffer (Life Technologies), frozen on dry ice and stored at -80°C until further use. The mRNA was purified using a Dynabeads mRNA DIRECT Purification Kit (Life Technologies) according to the manufacturer’s guidelines. Reverse transcription was performed with oligo(dT) primers (Thermo Scientific) or MARS-seq barcoded RT primers and the Affinity Script cDNA Synthesis Kit (Agilent).

Bulk RNA-sequencing

Bulk RNA-seq was performed according to a modified protocol of the original MARS-seq protocol *(49, 50)*. Briefly, mRNA was subjected to reverse transcription using an Affinity Script cDNA Synthesis Kit (Agilent) and MARS-seq barcoded RT primers. Samples were analyzed by qPCR and pooled according to their Ct values. Pooled samples were treated with Exonuclease I (New England BioLabs (NEB)) and size selected by a 1.2X AMPure XP beads (Beckman Coulter) cleanup. Second strand synthesis of the cDNA was performed using a second strand synthesis kit (NEB). Afterwards samples were subjected to *in vitro* transcription (IVT) with a HiScribe T7 RNA Polymerase kit (NEB). The DNA template was removed by Turbo DNase I (Life Technologies) treatment. Subsequently, the RNA was fragmented at 70°C using RNA fragmentation buffer (Invitrogen), and samples were purified

by 2X SPRI cleanup. Afterwards fragmented RNA ligation with MARS-seq ligation adapter was performed with T4 RNA ligase (NEB). In a second reverse transcription reaction using the MARS-seq RT2 primer and an Affinity Script cDNA Synthesis Kit (Agilent Technologies) the RNA was transcribed into cDNA. As final step the library was amplified in a nested PCR with P5_Rd1 and P7_Rd2 primers and Kapa HiFi Hotstart ready mix (Kapa Biosystems) and purified with a 0.7X AMPure XP beads cleanup. Library sizes and DNA concentration were determined using a TapeStation (Agilent Technologies) and a Qubit fluorometer (Life Technologies). The samples were sequenced using a NextSeq 500 system (Illumina).

ATAC-sequencing

For the preparation of ATAC-seq libraries 15,000-20,000 cells were used *(22)* as described earlier *(51)*. Briefly, nuclei were isolated by lysis with cold lysis buffer and centrifuged for 25min at 500xg and 4°C with low acceleration and brake using a swing-out rotor. The supernatant was carefully removed and nuclei were resuspended in 25µl reaction buffer containing 2µl of Tn5 transposase and 12.5µl of TD buffer (Nextera DNA library preparation kit; Illumina). The mix was incubated at 37°C for 1h. Afterwards, the DNA was purified by adding 5µl of cleanup buffer, 2µl of proteinase K (NEB) and 2µl of 5% SDS. After an incubation phase of 30min at 40°C, the tagmented DNA was enriched using AMPure XP beads (Beckman Coulter). The DNA was PCR-amplified with indexed primers and Kapa HiFi Hotstart ready mix (Kapa Biosystems). After the PCR, tagmented DNA fragments were selected for fragments smaller than 600bp and purified using AMPure XP beads. Libraries were subjected to a second PCR amplification with Kapa HiFi Hotstart ready mix (Kapa Biosystems), indexing primers and an appropriate number of reaction cycles depending on the library concentration. Library sizes and DNA concentration were determined using a TapeStation (Agilent Technologies) and a Qubit fluorometer (Life Technologies). Libraries were sequenced with an average of 20 million reads per sample on a NextSeq500 system (Illumina).

ChIPmentation

Preparation of ChIPmentation samples was performed according to *(21)*. $2x10^6$ AMs were BAL-isolated from C57BL/6 mice and fixed in a 1% PFA solution (in 10% FBS/PBS). The fixation reaction was quenched on ice by addition of glycine (125mM final concentration) and the samples were centrifuged at 300xg for 5min at 4°C. Subsequently cell pellets were washed twice with cold PBS and 1X Protease Inhibitor (Roche), snap-frozen in liquid nitrogen and stored at -80°C until further processing. The samples were thawed on ice and resuspended in Chromatin Prep Buffer (High Sensitivity Chromatin Preparation kit, Active Motif) with 1X Protease Inhibitor (Roche) before nuclei were released using a dounce

homogenizer with a tight pestel (Active Motif) and centrifuged at 4°C and 1250xg for 5min. Nuclei were then resuspended in cold Sonication Buffer and pipetted to facilitate nuclei disruption. The chromatin was sonicated using a Diagenode Bioruptor to achieve a fragment size ranging from 200-500bp. 1% of the sonicated chromatin was used for the INPUT sample, the rest was incubated overnight with pre-washed A Dynabeads (Thermofisher; previously blocked with 0.1% BSA) and 4µg of anti-C/EBPβ antibody (C-19; Santa Cruz Biotechnology). The following day, the beads were washed twice with RIPA-LS, twice with RIPA-HS, twice with RIPA-LiCl, twice with 10mM Tris-HCl pH 8.0 and finally resuspended and incubated in the Tagmentation Solution (0.25% Tagmentation Buffer, 2mM Tn5 (Illumina)) for 2min at 37°C. The tagmentation reaction was stopped on ice by adding cold RIPA-LS. Later, beads were washed twice in RIPA-LS, twice in 1X TE and finally resuspended in ChIP Elution Buffer. Samples were de-crosslinked overnight and purified on the following day using AMPure XP beads (NEB). Libraries were amplified using KAPA HiFi Hotstart ready mix (Kapa Biosystems) with published indexing primers (*22*) and finally purified using AMPure XP beads (NEB). Library sizes and DNA concentration were determined using a TapeStation (Agilent Technologies) and a Qubit fluorometer (Life Technologies). Libraries were sequenced with an average of 30 million reads per sample on a NextSeq500 system (Illumina). The experiment was performed in duplicates.

Processing and analysis of ATAC-seq data

ATAC-seq reads were aligned to the mouse genome v. GRCm38 using the BWA-MEM algorithm implemented in the bwa program *(52)*, v. 0.7.17. Peaks were called with MACS2, v. 2.2.7.1 and processed with the R package DiffBind (v. 2.14) *(53, 54)*. Differential binding analysis was performed using the DESeq2 R package (v. 1.26; *(55)*). ChIPseeker v. 1.22.1 was used for peak annotation *(56)*. For each comparison, significant peaks were defined as those with $|\log2FC| > 2$ and adj. p-value < 0.05. For motif search and annotation, the MEME suite (v. 5.0.5) was used. Motifs were first identified using DREME by comparing differential peak sequences to background sequences, separately for up- and down-regulated peaks. Then, identified motifs were annotated using the TOMTOM program and the Jaspar2020 database *(57)*. For comparison between RNA-seq and ATAC-seq data, the R package disco (v. 0.6; *(58)*) was used to calculate the “disco score”, a heuristic metric based on p-values and log2FC in both comparisons. Disco score takes extreme values for features that are either significantly regulated in the same direction in both comparisons (“concordant” features) or significantly regulated in opposite direction in the two comparisons (“discordant” features).

Processing and analysis of RNA-seq and microarray data

We used fastuniq *(59)* to collapse PCR duplicates and STAR v2.6.1a *(60)* to align unique reads to the mouse genome (GRCm38). Gene expression was quantified using featureCounts v1.6.3 *(61)* and the Gencode vM12 reference. We then used DESeq2 v1.24 *(55)* on selected sample groups to perform differential expression between all pairs of conditions, with ashr shrinkage *(62)*. Genes with adj. p-value < 0.01 and $|\log2FC| > 1$ were selected, and z-scores of log2 counts-per-million (CPM) values were computed to construct a heatmap with ComplexHeatmap v2.0.0 *(63)*, perform PC analysis, and cluster genes using kmeans. Gene set enrichment using gene sets from Gene Ontology and KEGG was performed for each cluster with ClusterProfiler v3.12 *(64)* using all genes with mean CPM > 1 as background.

For fig. S5, we downloaded microarray data of CD11c-Cre *Pparg* flox and control AMs from GEO (GSE60249) using the GEOquery package and averaged expression values over all probes for a given gene. We then combined log2(1+CPM) values from RNA-seq with microarray expression values, removing a batch effect between RNA-seq and microarray data with ComBat *(65)* after quantile normalization restricted to the intersection of the top 95% of genes from each dataset. We then performed differential expression analysis between pairs of conditions using limma v3.40.6 *(66)*.

Processing and analysis of ChIPmentation data

ChIPmentation data was analyzed with the Pigx pipeline for ChIP-seq data, which comprised a read trimming with Trim Galore, read mapping to mm10 with Bowtie2 and peak calling done by MACS *(53, 54)*. We filtered the resulting peaks by FDR with a cutoff of 1e-05 and merged them using Diffbind *(53, 54)* while retaining only those peaks found in both samples. This resulted in 18694 peaks annotated with 7604 genes using GREAT. A coverage map of the 18694 peaks was prepared with deeptools. We overlapped the annotated ChIP genes with genes deregulated in WT vs. *Cebpb*-deficient adult AMs (Fig. 2D). To assess the significance of overlaps shown in the Venn diagram (Fig. 6B) a Fisher test was applied.

Western blot

AMs were isolated by BAL and lysed with RIPA buffer supplemented with 1X cOmplete ULTRA protease inhibitor cocktail (Roche) and 1mM DTT for 10min on ice. Subsequently protein lysates were sonicated in an ultrasonic water bath for 20sec and centrifuged at 14000rpm and 4°C for 10min. The supernatant was transferred to a new tube and incubated with SDS loading buffer at 95°C for 5min before proteins were separated by electrophoresis on a 4-15% Criterion TGX precast gel (Bio-Rad) at 100-130V in SDS running buffer. Proteins were blotted onto a nitrocellulose membrane using the Trans-Blot Turbo System (Bio-Rad) at 2.5Amp and 25V for 10min and the membrane blocked in milk TBS-T for 1h. Following

overnight incubation at 4°C with a 1:500 dilution of rabbit-anti-C/EBPβ (C-19; Santa Cruz Biotechnology) antibody in milk TBS-T, the membrane was washed with TBS-T 4 times for 5min and incubated with secondary antibody solution (1:5000 ECL anti-rabbit IgG (GE Healthcare) in milk TBS-T) for 1h at room temperature. The membrane was again washed with TBS-T 4 times for 5min before protein signals were detected using Immobilon Western Chemiluminescent HRP substrate (Millipore).

Quantitative real-time PCR (qPCR)

qPCR of mouse cDNA was performed using PowerUp SYBR Green Mastermix (Thermo Fisher Scientific) and the following primers: *Actb* (5'-GGAGATTACTGCTCTGGCTCC-3' and 5'-AGGGTGTAAAACGCAGCTC-3'), *Cebpb* (5'-TCGGGACTTGATGCAATCC-3' and 5'-AAACATCAACAACCCCGC-3'), *Pparg1* (5'-AAGAAGCGGTGAACCACTGA-3' and 5'-GGAATGCGAGTGGTCTTCCA-3'), *Pparg2* (5'-TCGCTGATGCACTGCCTATG-3' and 5'-CGAGTGGTCTTCCATCACGG-3'). Reactions were performed in 10µl reaction volumes on a QuantStudio 6 Flex Real-Time PCR System (Thermo Fisher Scientific). All analyzed expression levels were normalized to *Actb* expression.

In vitro culture and treatment of Mx-Cre AMs

AMs were isolated by BAL, seeded in RPMI complete medium in non-tissue culture treated 12-well plates and incubated at 37°C to allow the AMs to adhere. After 4h the medium was exchanged to remove non-adherent cells. AMs were cultured in RPMI complete medium supplemented with 20ng/ml CSF2 (Stemcell Technologies) for 7 days to expand the cells. Every 2 to 3 days the medium was replaced. At day 7 a fraction of the AMs was harvested for analysis, while the remaining cells were treated with 1000units/ml of mouse IFNα (Miltenyi) to induce Cre-mediated recombination. IFNα treatment was repeated twice in two-day intervals (see fig. 3B). At day 14 all cells were harvested for analysis.

In vitro culture of bone marrow cells, PMs and AMs

BM cells were flushed from femur and tibia, washed and red blood cells were lysed. $2x10^5$ cells were resuspended in 1.5ml RPMI complete medium supplemented with 20ng/ml CSF2 (Stemcell Technologies) and cells were cultured in non-tissue culture treated 6-well plates. Every second day the medium was exchanged. At day 7, cells were harvested, centrifuged, lysed with RNA lysis buffer (Life Technologies) and frozen until further processing for RNA isolation.

PMs were isolated by FACS from peritoneal lavage and cultured in RPMI complete medium supplemented with 20ng/ml CSF2 or 20ng/ml CSF1 (both Stemcell Technologies) in non-

tissue culture treated 12-well plates. After 48h the cells were lysed with RNA lysis buffer (Life Technologies), frozen on dry ice and stored at -80°C until further use.
AMs were isolated by BAL, seeded in RPMI complete medium in non-tissue culture treated 12-well plates and incubated at 37°C to allow AMs to adhere. After 4h the medium was exchanged to remove non-adherent cells. AMs were cultured in RPMI complete medium without or supplemented with 20ng/ml CSF2 (Stemcell Technologies), 20ng/ml CSF2 together with 1µM Ruxolitinib (Tocris) or 20ng/ml CSF1 (Stemcell Technologies) according to the respective experimental setup. After 48h cells were harvested for RNA isolation as described above.

Luciferase reporter assay

Genomic regions of the *Pparg* locus were cloned from C57BL/6 DNA. The following primers were used to clone the *Pparg1* promoter: forward: 5'-TTCTCGAGCCCTCTCCACCCTATGTGT-3'; reverse: 5'-GTAAGCTTGTCGTCACACTCGGT-3'; the *Pparg2* promoter: forward: AGGACTCGAGCTTTTGTTCTATTCT; reverse: 5'-CCAAAGCTTCACCCATAACAGCATAAA-3' and the *Pparg* enhancer fragment: forward: 5'-GTGAGCTCTAGGATTCTGTATTCAGC-3'; reverse: 5'-TCCTCGAGGTGAGAATTTTAGTCAAGT-3'. The promoter fragments were cloned via XhoI/HindIII digest into the pGL4.10 (Promega) luciferase vector. The enhancer was cloned via SacI/XhoI digest either alone or in front of the *Pparg*2 promoter into pGL4.10. All clones were sequenced to verify cloning and sequences. For transfection, $1x10^4$ *Cebpb*-deficient MEF cells were plated into 96-well plates. The next day, 50ng of test luciferase vector and different combinations of 50ng pcDNA3.1 (Addgene) containing either no gene (control), or LAP*, LAP or LIP were mixed in were mixed in 5µl serum free medium. To control for transfection efficiency, 12.5ng Renilla luciferase (pGL4.70; Promega) was added. Afterwards, 5µl serum free medium containing 1.1µl 7.5mM PEI (DNA:PEI ratio 1:10) was added to the mix and incubated for 10min. 10µl transfection mix was carefully added to each well. Firefly luciferase and Renilla luciferase activity was measured with Luc-Pair™ Duo-Luciferase HT Assay Kit (Genecopoeia) 48h after transfection according to the manufacturer's protocol. A Berthold Luminometer (Centro LB 960) was used for measurement. All analysis was performed in duplicates and all experiments were repeated twice with similar results.

Quantification and statistical analysis

Statistical analysis (with exception of RNA-seq, ATAC-seq, ChIPmentation and lipidomic analysis; see respective methods sections for these analyses) was performed using the GraphPad Prism 6 software and statistical tests were chosen according to assumptions

considering data distribution and variance characteristics. To evaluate statistical differences between two groups a two-tailed t test with Welch's correction was applied. For comparison of three groups a one-way ANOVA test was used followed by multiple comparison correction with a Tukey test (in case of comparison of each group against every other group) or Dunnett test (in case of comparison of all groups against a control group). Data in all experiments are depicted as mean ± standard deviation (SD) and statistical significance is presented as: n.s. $p > 0.05$; *$p < 0.05$; **$p < 0.01$; ***$p < 0.001$. N indicates the number of animals used in the experiment and each dot in the graphs corresponds to one animal.

Supplementary materials

Figure S1. Gating strategy for the identification of AMs and other TRMs

Figure S2. Influence of housing condition and sex on the transcriptome of *Cebpb*-deficient AMs.

Figure S3. Analysis of AMs from conditional *Cebpb*-deficient mice.

Figure S4. Chromatin accessibility in the promoter regions of *Cebpb*$^{-/-}$ and LIP AMs

Figure S5. Comparison of *Cebpb*$^{-/-}$ AMs and *Pparg*-deficient AMs

Figure S6. *Cebpb* expression is unaffected in *Csf2rb*-deficient pre-AMs.

Figure S7. CSF2 and C/EBPβ are necessary co-factors for the induction of *Pparg2* in other macrophage subsets.

Supplementary data 1. RNA-sequencing results of *Cebpb*-deficient fetal monocytes, pre-AMs and adult AMs and controls. Related to Fig. 2.

Supplementary data 2. RNA-sequencing results of *Cebpb*-deficient AMs isolated from adult constitutive KO animals (*Cebpb*$^{-/-}$) and different conditional Cre mice (CD11c-Cre *Cebpb*$^{fl/fl}$ or LyzM-Cre *Cebpb*$^{fl/fl}$). Related to fig. S3.

Supplementary data 3. RNA-sequencing results of AMs isolated from *Cebpb*$^{-/-}$, LIP (*Cebpb*$^{LIP/LIP}$) mice and respective controls. Related to Fig. 5.

Supplementary data 4: Significantly bound chromatin regions as determined by C/EBPβ ChIPmentation. Related to Fig. 6A-E.

Supplementary data 5: ATAC-sequencing results of AMs isolated from *Cebpb*$^{-/-}$ mice and respective controls. Related to Fig. 6F,G.

Supplementary data 6: ATAC-sequencing results of AMs isolated from LIP (*Cebpb*$^{LIP/LIP}$) mice and respective controls. Related to Fig. 6F,G.

Supplementary data 7: Transcriptome comparison of *Csf2rb*-deficient pre-AMs against *Cebpb*$^{-/-}$ pre-AMs with respective controls. Related to fig. S6.

References

1. T. Hussell, T. J. Bell, Alveolar macrophages: plasticity in a tissue-specific context, *Nat. Rev. Immunol.* **14**, 81–93 (2014).

2. B. C. Trapnell, J. A. Whitsett, K. Nakata, Pulmonary alveolar proteinosis, *N. Engl. J. Med.* **349**, 2527–2539 (2003).

3. D. Hashimoto, A. Chow, C. Noizat, P. Teo, M. B. Beasley, M. Leboeuf, C. D. Becker, P. See, J. Price, D. Lucas, M. Greter, A. Mortha, S. W. Boyer, E. C. Forsberg, M. Tanaka, N. van Rooijen, A. García-Sastre, E. R. Stanley, F. Ginhoux, P. S. Frenette, M. Merad, Tissue-resident macrophages self-maintain locally throughout adult life with minimal contribution from circulating monocytes, *Immunity* **38**, 792–804 (2013).

4. M. Guilliams, I. De Kleer, S. Henri, S. Post, L. Vanhoutte, S. De Prijck, K. Deswarte, B. Malissen, H. Hammad, B. N. Lambrecht, Alveolar macrophages develop from fetal monocytes that differentiate into long-lived cells in the first week of life via GM-CSF, *J. Exp. Med.* **210**, 1977–1992 (2013).

5. M. Cohen, A. Giladi, A.-D. Gorki, D. G. Solodkin, M. Zada, A. Hladik, A. Miklosi, T.-M. Salame, K. B. Halpern, E. David, S. Itzkovitz, T. Harkany, S. Knapp, I. Amit, Lung Single-Cell Signaling Interaction Map Reveals Basophil Role in Macrophage Imprinting, *Cell* **175**, 1031–1044.e18 (2018).

6. V. Goss, A. N. Hunt, A. D. Postle, Regulation of lung surfactant phospholipid synthesis and metabolism, *Biochim. Biophys. Acta* **1831**, 448–458 (2013).

7. C. Schneider, S. P. Nobs, M. Kurrer, H. Rehrauer, C. Thiele, M. Kopf, Induction of the nuclear receptor PPAR-γ by the cytokine GM-CSF is critical for the differentiation of fetal monocytes into alveolar macrophages, *Nature Immunology* **15**, 1026–1037 (2014).

8. M. Straccia, N. Gresa-Arribas, G. Dentesano, A. Ejarque-Ortiz, J. M. Tusell, J. Serratosa, C. Solà, J. Saura, Pro-inflammatory gene expression and neurotoxic effects of activated microglia are attenuated by absence of CCAAT/enhancer binding protein β, *J Neuroinflammation* **8**, 156 (2011).

9. A. Ndoja, R. Reja, S.-H. Lee, J. D. Webster, H. Ngu, C. M. Rose, D. S. Kirkpatrick, Z. Modrusan, Y.-J. J. Chen, D. L. Dugger, V. Gandham, L. Xie, K. Newton, V. M. Dixit, Ubiquitin Ligase COP1 Suppresses Neuroinflammation by Degrading c/EBPβ in Microglia, *Cell* **182**, 1156–1169.e12 (2020).

10. H. Hirai, P. Zhang, T. Dayaram, C. J. Hetherington, S.-I. Mizuno, J. Imanishi, K. Akashi, D. G. Tenen, C/EBPbeta is required for “emergency” granulopoiesis, *Nature Immunology* **7**, 732–739 (2006).

11. A. Mildner, J. Schönheit, A. Giladi, E. David, D. Lara-Astiaso, E. Lorenzo-Vivas, F. Paul, L. Chappell-Maor, J. Priller, A. Leutz, I. Amit, S. Jung, Genomic Characterization of Murine Monocytes Reveals C/EBPβ Transcription Factor Dependence of Ly6C(-) Cells, *Immunity* **46**, 849–862.e7 (2017).

12. D. W. Cain, E. G. O'Koren, M. J. Kan, M. Womble, G. D. Sempowski, K. Hopper, M. D. Gunn, G. Kelsoe, Identification of a tissue-specific, C/EBPβ-dependent pathway of differentiation for murine peritoneal macrophages, *J. Immunol.* **191**, 4665–4675 (2013).

13. E. L. Gautier, T. Shay, J. Miller, M. Greter, C. Jakubzick, S. Ivanov, J. Helft, A. Chow, K. G. Elpek, S. Gordonov, A. R. Mazloom, A. Ma'ayan, W.-J. Chua, T. H. Hansen, S. J. Turley, M. Merad, G. J. Randolph, Immunological Genome Consortium, Gene-expression profiles and transcriptional regulatory pathways that underlie the identity and diversity of mouse tissue macrophages, *Nature Immunology* **13**, 1118–1128 (2012).

14. Z. Liu, Y. Gu, S. Chakarov, C. Bleriot, I. Kwok, X. Chen, A. Shin, W. Huang, R. J. Dress, C.-A. Dutertre, A. Schlitzer, J. Chen, L. G. Ng, H. Wang, Z. Liu, B. Su, F. Ginhoux, Fate Mapping via Ms4a3-Expression History Traces Monocyte-Derived Cells, *Cell* **178**, 1509–1525.e19 (2019).

15. Z. Liu, Y. Gu, S. Chakarov, C. Bleriot, X. Chen, A. Shin, W. Huang, R. J. Dress, C.-A. Dutertre, A. Schlitzer, J. Chen, H. Wang, Z. Liu, B. Su, F. Ginhoux, Fate mapping via Ms4a3 expression history

traces monocyte-derived cells, *bioRxiv*, 652032 (2019).

16. R. Kühn, F. Schwenk, M. Aguet, K. Rajewsky, Inducible gene targeting in mice, *Science* **269**, 1427–1429 (1995).

17. C. L. Abram, G. L. Roberge, Y. Hu, C. A. Lowell, Comparative analysis of the efficiency and specificity of myeloid-Cre deleting strains using ROSA-EYFP reporter mice, *J Immunol Methods* **408**, 89–100 (2014).

18. L. van de Laar, W. Saelens, S. De Prijck, L. Martens, C. L. Scott, G. Van Isterdael, E. Hoffmann, R. Beyaert, Y. Saeys, B. N. Lambrecht, M. Guilliams, Yolk Sac Macrophages, Fetal Liver, and Adult Monocytes Can Colonize an Empty Niche and Develop into Functional Tissue-Resident Macrophages, *Immunity* **44**, 755–768 (2016).

19. K. Wethmar, J. J. Smink, A. Leutz, Upstream open reading frames: molecular switches in (patho)physiology, *Bioessays* **32**, 885–893 (2010).

20. V. Bégay, J. J. Smink, C. Loddenkemper, K. Zimmermann, C. Rudolph, M. Scheller, D. Steinemann, U. Leser, B. Schlegelberger, H. Stein, A. Leutz, Deregulation of the endogenous C/EBPβ LIP isoform predisposes to tumorigenesis, *J Mol Med (Berl)* **93**, 39–49 (2015).

21. C. Schmidl, A. F. Rendeiro, N. C. Sheffield, C. Bock, ChIPmentation: fast, robust, low-input ChIP-seq for histones and transcription factors, *Nat. Methods* **12**, 963–965 (2015).

22. J. D. Buenrostro, P. G. Giresi, L. C. Zaba, H. Y. Chang, W. J. Greenleaf, Transposition of native chromatin for fast and sensitive epigenomic profiling of open chromatin, DNA-binding proteins and nucleosome position, *Nat. Methods* **10**, 1213–1218 (2013).

23. A. Shemer, J. Grozovski, T. L. Tay, J. Tao, A. Volaski, P. Süß, A. Ardura-Fabregat, M. Gross-Vered, J.-S. Kim, E. David, L. Chappell-Maor, L. Thielecke, C. K. Glass, K. Cornils, M. Prinz, S. Jung, Engrafted parenchymal brain macrophages differ from microglia in transcriptome, chromatin landscape and response to challenge, *Nat Commun* **9**, 5206 (2018).

24. A. Vidal-Puig, M. Jimenez-Liñan, B. B. Lowell, A. Hamann, E. Hu, B. Spiegelman, J. S. Flier, D. E. Moller, Regulation of PPAR gamma gene expression by nutrition and obesity in rodents, *J. Clin. Invest.* **97**, 2553–2561 (1996).

25. E. M. Todd, J. Y. Zhou, T. P. Szasz, L. E. Deady, J. A. D'Angelo, M. D. Cheung, A. H. J. Kim, S. C. Morley, Alveolar macrophage development in mice requires L-plastin for cellular localization in alveoli, *Blood* **128**, 2785–2796 (2016).

26. M. I. Lefterova, Y. Zhang, D. J. Steger, M. Schupp, J. Schug, A. Cristancho, D. Feng, D. Zhuo, C. J. Stoeckert, X. S. Liu, M. A. Lazar, PPARgamma and C/EBP factors orchestrate adipocyte biology via adjacent binding on a genome-wide scale, *Genes Dev* **22**, 2941–2952 (2008).

27. S. Watanabe, T. Itoh, K. Arai, Roles of JAK kinases in human GM-CSF receptor signal transduction, *J Allergy Clin Immunol* **98**, S183–91 (1996).

28. A. Mortha, A. Chudnovskiy, D. Hashimoto, M. Bogunovic, S. P. Spencer, Y. Belkaid, M. Merad, Microbiota-dependent crosstalk between macrophages and ILC3 promotes intestinal homeostasis, *Science* **343**, 1249288–1249288 (2014).

29. L. Robb, C. C. Drinkwater, D. Metcalf, R. Li, F. Köntgen, N. A. Nicola, C. G. Begley, Hematopoietic and lung abnormalities in mice with a null mutation of the common beta subunit of the receptors for granulocyte-macrophage colony-stimulating factor and interleukins 3 and 5, *Proc. Natl. Acad. Sci. U.S.A.* **92**, 9565–9569 (1995).

30. B. Becher, A. Schlitzer, J. Chen, F. Mair, H. R. Sumatoh, K. W. W. Teng, D. Low, C. Ruedl, P. Riccardi-Castagnoli, M. Poidinger, M. Greter, F. Ginhoux, E. W. Newell, High-dimensional analysis of the murine myeloid cell system, *Nature Immunology* **15**, 1181–1189 (2014).

1026 31. X. Ma, D. Wang, W. Zhao, L. Xu, Deciphering the Roles of PPARγ in Adipocytes via Dynamic
1027 Change of Transcription Complex, *Front Endocrinol (Lausanne)* **9**, 473 (2018).

1028 32. J. E. Merrett, T. Bo, P. J. Psaltis, C. G. Proud, Identification of DNA response elements regulating
1029 expression of CCAAT/enhancer-binding protein (C/EBP) β and δ and MAP kinase-interacting kinases
1030 during early adipogenesis, *Adipocyte* **9**, 427–442 (2020).

1031 33. D. J. Steger, G. R. Grant, M. Schupp, T. Tomaru, M. I. Lefterova, J. Schug, E. Manduchi, C. J.
1032 Stoeckert, M. A. Lazar, Propagation of adipogenic signals through an epigenomic transition state,
1033 *Genes Dev* **24**, 1035–1044 (2010).

1034 34. T. Tanaka, N. Yoshida, T. Kishimoto, S. Akira, Defective adipocyte differentiation in mice lacking
1035 the C/EBPbeta and/or C/EBPdelta gene, *EMBO J.* **16**, 7432–7443 (1997).

1036 35. D. Ren, T. N. Collingwood, E. J. Rebar, A. P. Wolffe, H. S. Camp, PPARgamma knockdown by
1037 engineered transcription factors: exogenous PPARgamma2 but not PPARgamma1 reactivates
1038 adipogenesis, *Genes Dev* **16**, 27–32 (2002).

1039 36. Q.-Q. Tang, M. Grønborg, H. Huang, J.-W. Kim, T. C. Otto, A. Pandey, M. D. Lane, Sequential
1040 phosphorylation of CCAAT enhancer-binding protein beta by MAPK and glycogen synthase kinase
1041 3beta is required for adipogenesis, *Proc. Natl. Acad. Sci. U.S.A.* **102**, 9766–9771 (2005).

1042 37. C. Nieto, R. Bragado, C. Municio, E. Sierra-Filardi, B. Alonso, M. M. Escribese, J. Domínguez-
1043 Andrés, C. Ardavín, A. Castrillo, M. A. Vega, A. Puig-Kröger, A. L. Corbí, The Activin A-Peroxisome
1044 Proliferator-Activated Receptor Gamma Axis Contributes to the Transcriptome of GM-CSF-
1045 Conditioned Human Macrophages, *Front Immunol* **9**, 31 (2018).

1046 38. Y. Lavin, D. Winter, R. Blecher-Gonen, E. David, H. Keren-Shaul, M. Merad, S. Jung, I. Amit,
1047 Tissue-resident macrophage enhancer landscapes are shaped by the local microenvironment, *Cell*
1048 **159**, 1312–1326 (2014).

1049 39. C. Bornstein, D. Winter, Z. Barnett-Itzhaki, E. David, S. Kadri, M. Garber, I. Amit, A negative
1050 feedback loop of transcription factors specifies alternative dendritic cell chromatin States, *Mol. Cell* **56**,
1051 749–762 (2014).

1052 40. R. Siersbæk, R. Nielsen, S. John, M.-H. Sung, S. Baek, A. Loft, G. L. Hager, S. Mandrup,
1053 Extensive chromatin remodelling and establishment of transcription factor “hotspots” during early
1054 adipogenesis, *EMBO J.* **30**, 1459–1472 (2011).

1055 41. V. Bégay, C. Baumeier, K. Zimmermann, A. Heuser, A. Leutz, The C/EBPβ LIP isoform rescues
1056 loss of C/EBPβ function in the mouse, *Sci Rep* **8**, 8417–10 (2018).

1057 42. C.-H. Lee, R. M. Evans, Peroxisome proliferator-activated receptor-gamma in macrophage lipid
1058 homeostasis, *Trends Endocrinol Metab* **13**, 331–335 (2002).

1059 43. E. L. Gautier, A. Chow, R. Spanbroek, G. Marcelin, M. Greter, C. Jakubzick, M. Bogunovic, M.
1060 Leboeuf, N. van Rooijen, A. J. Habenicht, M. Merad, G. J. Randolph, Systemic analysis of PPARγ in
1061 mouse macrophage populations reveals marked diversity in expression with critical roles in resolution
1062 of inflammation and airway immunity, *J. Immunol.* **189**, 2614–2624 (2012).

1063 44. J. C. Cronk, A. J. Filiano, A. Louveau, I. Marin, R. Marsh, E. Ji, D. H. Goldman, I. Smirnov, N.
1064 Geraci, S. Acton, C. C. Overall, J. Kipnis, Peripherally derived macrophages can engraft the brain
1065 independent of irradiation and maintain an identity distinct from microglia, *J. Exp. Med.* **215**, 1627–
1066 1647 (2018).

1067 45. E. Sterneck, L. Tessarollo, P. F. Johnson, An essential role for C/EBPbeta in female reproduction,
1068 *Genes Dev* **11**, 2153–2162 (1997).

1069 46. B. E. Clausen, C. Burkhardt, W. Reith, R. Renkawitz, I. Förster, Conditional gene targeting in
1070 macrophages and granulocytes using LysMcre mice, *Transgenic Res* **8**, 265–277 (1999).

1071 47. P. B. Stranges, J. Watson, C. J. Cooper, C.-M. Choisy-Rossi, A. C. Stonebraker, R. A. Beighton, H.
1072 Hartig, J. P. Sundberg, S. Servick, G. Kaufmann, P. J. Fink, A. V. Chervonsky, Elimination of antigen-
1073 presenting cells and autoreactive T cells by Fas contributes to prevention of autoimmunity, *Immunity*
1074 **26**, 629–641 (2007).

1075 48. E. Sterneck, S. Zhu, A. Ramirez, J. L. Jorcano, R. C. Smart, Conditional ablation of C/EBP beta
1076 demonstrates its keratinocyte-specific requirement for cell survival and mouse skin tumorigenesis,
1077 *Oncogene* **25**, 1272–1276 (2006).

1078 49. D. A. Jaitin, E. Kenigsberg, H. Keren-Shaul, N. Elefant, F. Paul, I. Zaretsky, A. Mildner, N. Cohen,
1079 S. Jung, A. Tanay, I. Amit, Massively Parallel Single-Cell RNA-Seq for Marker-Free Decomposition of
1080 Tissues into Cell Types, *Science* **343**, 776–779 (2014).

1081 50. E. M. Lyras, K. Zimmermann, L. K. Wagner, D. Dörr, C. S. N. Klose, C. Fischer, S. Jung, S. Yona,
1082 A.-H. Hovav, W. Stenzel, S. Dommerich, T. Conrad, A. Leutz, A. Mildner, Tongue immune
1083 compartment analysis reveals spatial macrophage heterogeneity, *Elife* **11** (2022),
1084 doi:10.7554/eLife.77490.

1085 51. D. Lara-Astiaso, A. Weiner, E. Lorenzo-Vivas, I. Zaretsky, D. A. Jaitin, E. David, H. Keren-Shaul, A.
1086 Mildner, D. Winter, S. Jung, N. Friedman, I. Amit, Immunogenetics. Chromatin state dynamics during
1087 blood formation, *Science* **345**, 943–949 (2014).

1088 52. H. Li, Aligning sequence reads, clone sequences and assembly contigs with BWA-MEM (2013).

1089 53. R. Stark, G. B. R. P. version, 2011, DiffBind: differential binding analysis of ChIP-Seq peak data,
1090 *bioconductor.statistik.tu-dortmund.de*

1091 54. J. M. Gaspar, Improved peak-calling with MACS2, *bioRxiv*, 496521 (2018).

1092 55. M. I. Love, W. Huber, S. Anders, Moderated estimation of fold change and dispersion for RNA-seq
1093 data with DESeq2, *Genome Biol.* **15**, 1–21 (2014).

1094 56. G. Yu, L.-G. Wang, Q.-Y. He, ChIPseeker: an R/Bioconductor package for ChIP peak annotation,
1095 comparison and visualization, *Bioinformatics* **31**, 2382–2383 (2015).

1096 57. O. Fornes, J. A. Castro-Mondragon, A. Khan, R. van der Lee, X. Zhang, P. A. Richmond, B. P.
1097 Modi, S. Correard, M. Gheorghe, D. Baranašić, W. Santana-Garcia, G. Tan, J. Chèneby, B. Ballester,
1098 F. Parcy, A. Sandelin, B. Lenhard, W. W. Wasserman, A. Mathelier, JASPAR 2020: update of the
1099 open-access database of transcription factor binding profiles, *Nucleic Acids Res* **48**, D87–D92 (2020).

1100 58. T. Domaszewska, L. Scheuermann, K. Hahnke, H. Mollenkopf, A. Dorhoi, S. H. E. Kaufmann, J.
1101 Weiner, Concordant and discordant gene expression patterns in mouse strains identify best-fit animal
1102 model for human tuberculosis, *Sci Rep* **7**, 12094–13 (2017).

1103 59. H. Xu, X. Luo, J. Qian, X. Pang, J. Song, G. Qian, J. Chen, S. Chen, D. Doucet, Ed. FastUniq: a
1104 fast de novo duplicates removal tool for paired short reads, *PLoS ONE* **7**, e52249 (2012).

1105 60. A. Dobin, C. A. Davis, F. Schlesinger, J. Drenkow, C. Zaleski, S. Jha, P. Batut, M. Chaisson, T. R.
1106 Gingeras, STAR: ultrafast universal RNA-seq aligner, *Bioinformatics* **29**, 15–21 (2013).

1107 61. Y. Liao, G. K. Smyth, W. Shi, featureCounts: an efficient general purpose program for assigning
1108 sequence reads to genomic features, *Bioinformatics* **30**, 923–930 (2014).

1109 62. M. Stephens, False discovery rates: a new deal, *Biostatistics* **18**, 275–294 (2017).

1110 63. Z. Gu, R. Eils, M. Schlesner, Complex heatmaps reveal patterns and correlations in
1111 multidimensional genomic data, *Bioinformatics* **32**, 2847–2849 (2016).

1112 64. G. Yu, L.-G. Wang, Y. Han, Q.-Y. He, clusterProfiler: an R package for comparing biological
1113 themes among gene clusters, *OMICS* **16**, 284–287 (2012).

65. J. T. Leek, W. E. Johnson, H. S. Parker, A. E. Jaffe, J. D. Storey, The sva package for removing batch effects and other unwanted variation in high-throughput experiments, *Bioinformatics* **28**, 882–883 (2012).

66. M. E. Ritchie, B. Phipson, D. Wu, Y. Hu, C. W. Law, W. Shi, G. K. Smyth, limma powers differential expression analyses for RNA-sequencing and microarray studies, *Nucleic Acids Res* **43**, e47–e47 (2015).

Acknowledgments: We thank Victoria Malchin, Sarah Jaksch and Jermaine Voß for excellent technical support, as well as the MDC animal facility, especially Juliette Bergemann, the MDC FACS core unit, Hans-Peter Rahn, and the MDC genomic core facility, especially Daniele Sunaga-Franze. We thank Elisabeth Kowenz-Leutz for donation of C/EBP expression constructs and Ido Amit for support. The *Csf2rb*$^{-/-}$ line was kindly provided by Michael Sieweke (Center for Regenerative Therapies, Dresden, Germany). We also thank Clara Jana Lui Elender and Jérémy Favret for technical advice and Simon Yona and Steffen Jung for discussion. Computation has been performed on the HPC for Research cluster of the Berlin Institute of Health.

Funding: D.D. was funded by the international MDC PhD program and received a travel grant from Boehringer Ingelheim Fonds. A.M is a Heisenberg fellow supported by the DFG (MI1328/3-1).

Author contributions: D.D. performed most experiments and analysis. B.O. and J.W. were supervised by D.B. and performed bioinformatic analyses. A.M., L-K.W., E.M.L., V.S. and K.Z. helped with experiments and analysis. C.A. and D.J.L performed ChIPmentation experiments. R.L., D.L-A., F.P. and U.H. provided mouse lines and technical expertise. A.L. provided financial support, lab space, supervision, discussion, review and editing. A.M. designed and supervised the study. D.D. and A.M. wrote the manuscript.

Competing interests: The authors declare that they have no competing interests.

Data and code availability: All data needed to evaluate the conclusions in this article are present in the article or the Supplementary materials. Sequencing data that were generated within this study have been deposited in the Gene Expression Omnibus (GEO) database with the accession code GSE173970.

Microarray data of CD11c-Cre *Pparg* flox and control AMs used for transcriptomic comparison to *Cebpb* KO AMs were downloaded from GEO (GSE60249).

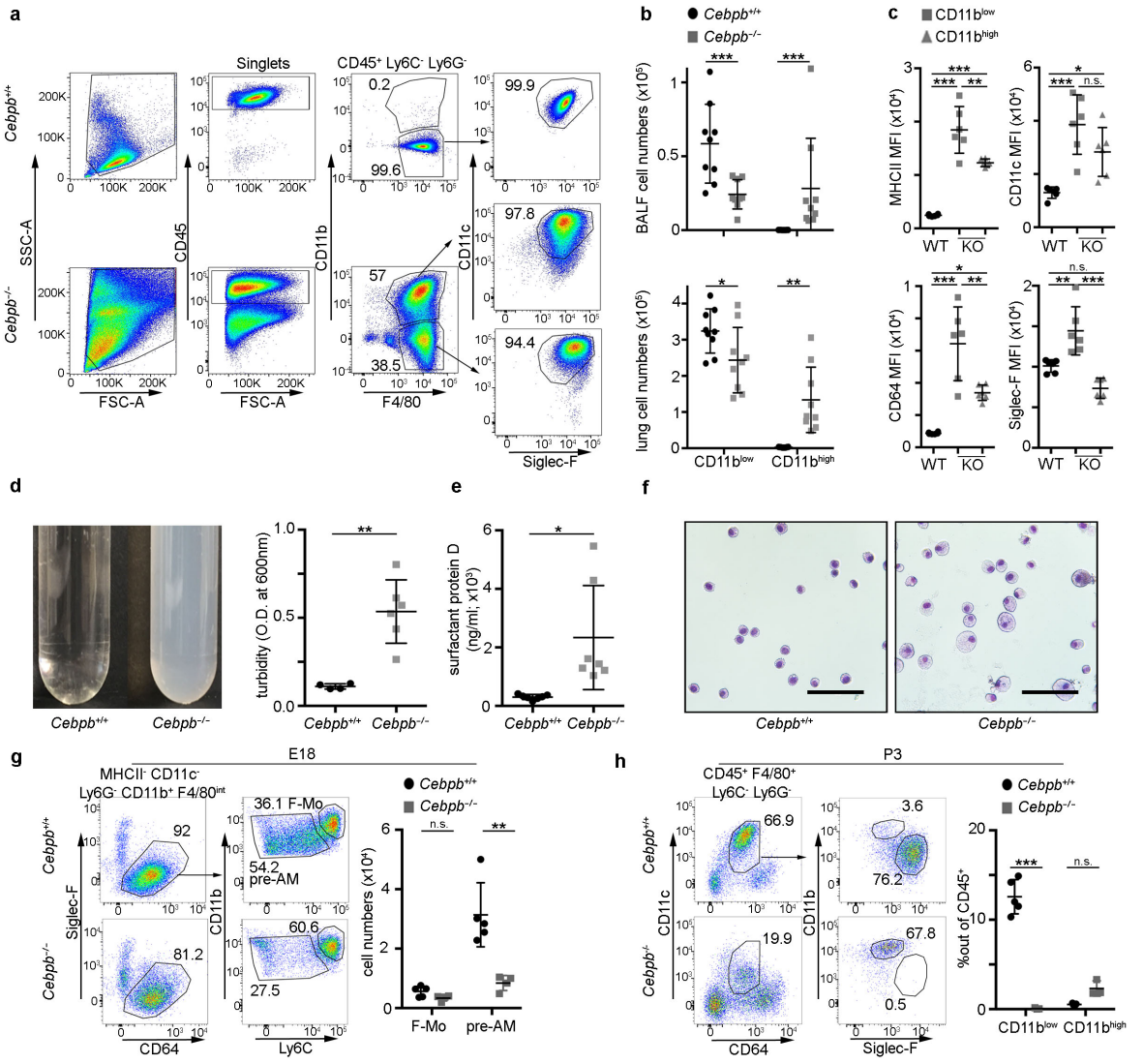

Figure 1

Figure 1. *Cebpb*-deficiency leads to PAP-like syndrome in mice.

(A) Representative flow cytometric analysis of lung cells isolated by bronchoalveloar lavage (BAL) from adult *Cebpb*$^{-/-}$ mice and littermate controls. Note that plots depict all cells detected in a complete BAL sample. **(B)** Quantification of absolute AM cell numbers in BAL fluid (upper panel) and lung tissue (lower panel; two experiments pooled). **(C)** Median fluorescence intensity (MFI) of CD64, Siglec-F, CD11c and MHCII as determined by flow cytometry in WT and CD11b^{low} and CD11b^{high} *Cebpb*-deficient AMs. **(D)** Turbidity of BAL fluid isolated from WT and *Cebpb*-deficient mice as assessed macroscopically (left panel) or by optical density measurement at 600nm (right panel). **(E)** Surfactant protein D concentration determined by ELISA in BAL fluid from *Cebpb*$^{-/-}$ mice and WT littermates (two experiments pooled). **(F)** Representative May–Grünwald–Giemsa staining of cytospins of AMs from *Cebpb*$^{-/-}$ mice and controls isolated by BAL. Scale bar = 50µm. **(G)** Exemplary flow cytometric analysis (left panel) and absolute cell numbers (right panel) of fetal lung Ly6C^{high} monocytes (F-Mo) and pre-AMs isolated from whole lung tissue of *Cebpb*-deficient and -proficient animals at E18. **(H)** Representative flow cytometric analysis (left panel) and

frequency quantification of $CD11c^+$ $CD64^+$ immature AMs out of $CD45^+$ cells (right panel; n=3-5 mice per genotype; mean ± SD) isolated from whole lung tissue of *Cebpb*-deficient and control animals at P3. Experiments in A-G were performed at least twice (n=3-6 mice per genotype and experiment; mean ± SD) with similar results. Each dot represents an individual mouse.

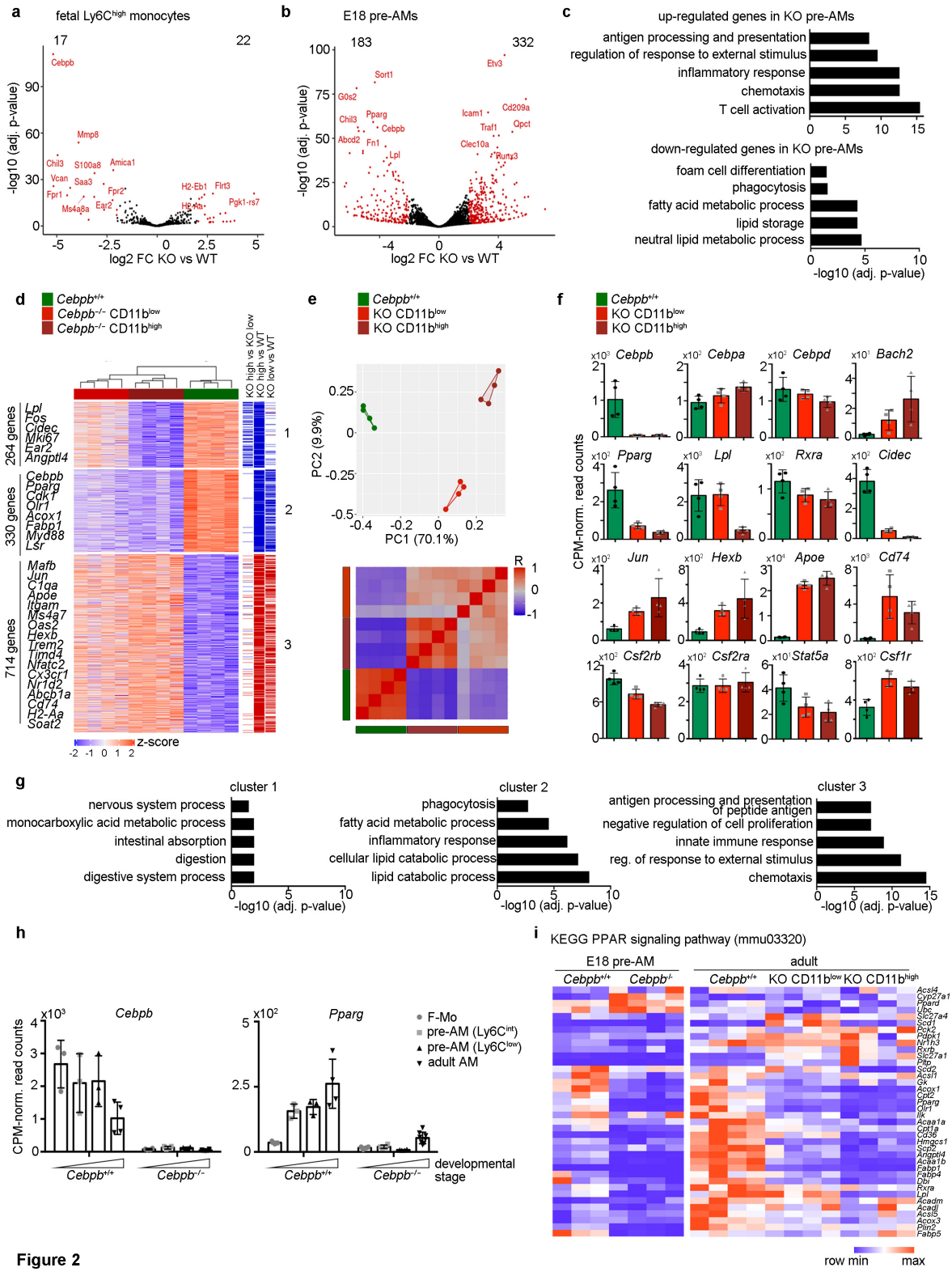

Figure 2

Figure 2. Transcriptomic analysis of embryonic and adult *Cebpb*-deficient AMs. **(A** and **B)** Lung Ly6C^{high} fetal monocytes and lung Ly6C^{low} pre-AMs were FACS-isolated from *Cebpb*-proficient (n=3) and -deficient (n=4) E18 mouse embryos and analyzed by RNA-seq. Depicted are all detected genes with DEGs (adj. p-value < 0.01 and |log2FC| > 2) marked in red. **(C)** Gene ontology enrichment analysis of the DEGs between *Cebpb*-deficient and

control pre-AMs. Shown are terms from the category 'biological process'. **(D)** AMs from WT littermates and CD11b^{high} and CD11b^{low} AMs from adult *Cebpb*-deficient mice were isolated by FACS and analyzed by RNA-seq (n=4 mice per genotype). Shown are genes with an adj. p-value < 0.01 and |log2FC| > 1 in at least one pairwise comparison. Columns on the right hand of the heatmap indicate significantly differential genes in the indicated contrasts. Significantly upregulated genes are marked in red, significantly downregulated genes are marked in blue. **(E)** Principal component analysis (upper panel) and correlation matrix (lower panel) of the three cell populations described in D. **(F)** Normalized CPM read counts of AM genes of interest (mean ± SD). **(G)** Gene ontology enrichment analysis of the three clusters depicted in D. Only biological process terms are shown. **(H)** Normalized CPM read counts of *Cebpb* and *Pparg* expression in fetal monocytes (F-Mo), pre-AM I (Ly6C^{int}), pre-AM II (Ly6C^{low}) and adult AMs isolated from WT and *Cebpb*-deficient mice. **(I)** Heatmap showing the expression of genes involved in the KEGG PPAR signaling pathway (mmu03320) in *Cebpb*-deficient and -proficient E18 pre-AMs and adult AMs. Shown are only genes that were detected with >10 reads in at least one group. See also Suppl. Data 1 for full description of DEGs in F-Mo, pre-AMs and adult AMs.

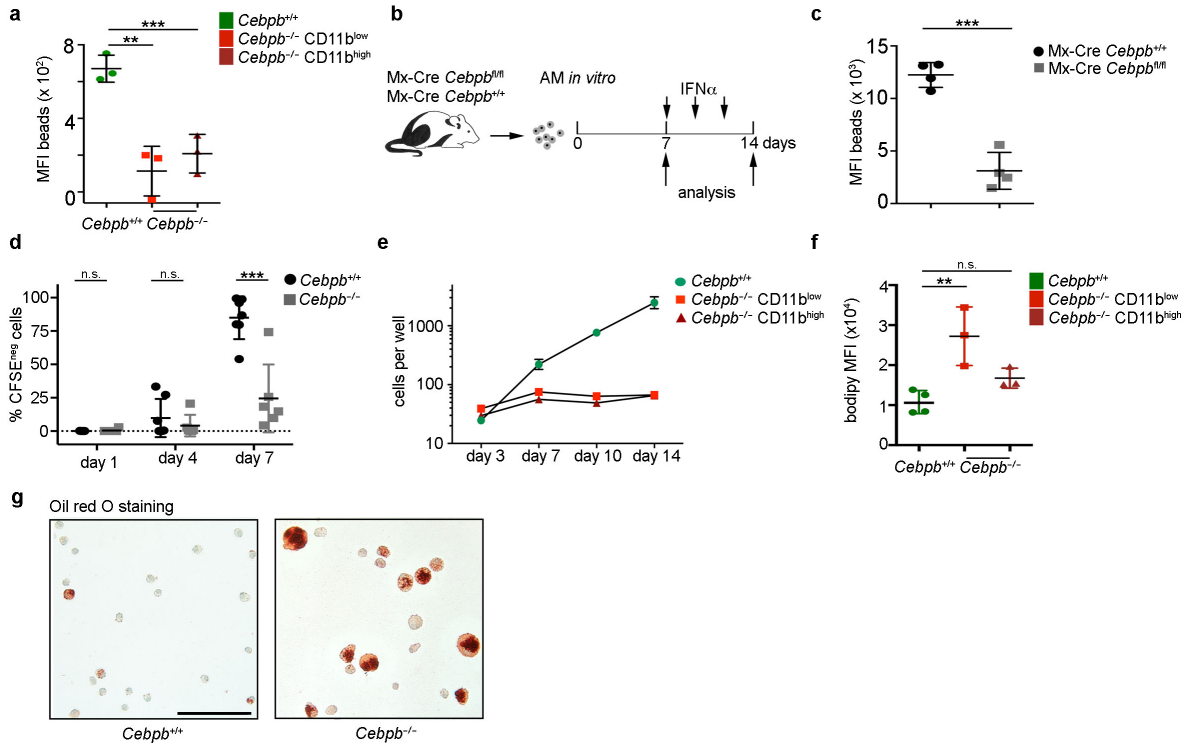

Figure 3

Figure 3. Functional impairment of adult *Cebpb*-deficient AMs.

(A) Latex bead phagocytosis of WT (green) and CD11b^{high} (dark red) or CD11b^{low} (light red) *Cebpb*$^{-/-}$ AMs was analyzed by flow cytometry. **(B)** Schematic of Mx-Cre experiment. BAL-isolated AMs were cultured with CSF2 for 7 days before IFNα was added a total of three times in two-day intervals. Analysis was performed at day 14. **(C)** Latex bead phagocytosis of Mx-Cre *Cebpb*$^{+/+}$ control (black) and Mx-Cre *Cebpb*$^{fl/fl}$ AMs (grey). Shown is the MFI of phagocytosed beads as determined by flow cytometry. **(D)** CFSE analysis of wildtype and *Cebpb*$^{-/-}$ AMs. Cells were cultured for 1, 4 and 7 days with CSF2 and analyzed by flow cytometry. Quantification of CFSE^{neg} cell frequency from two pooled experiments. **(E)** Quantification of *in vitro*-cultured AMs. AMs from WT controls (green) and CD11b^{high} (dark red) and CD11b^{low} (light red) AMs from *Cebpb*$^{-/-}$ mice were sorted into 96-well plates in triplicates and cultured with CSF2. Cell numbers were tracked by microscopy at day 3, 7, 10 and 14 after seeding (n=4 mice per genotype). **(F)** WT (green) and CD11b^{high} (dark red) and CD11b^{low} *Cebpb*$^{-/-}$ (light red) AMs were loaded with bodipy and the MFI of bodipy was analyzed by flow cytometry . **(G)** Oil Red O staining of WT (left) and *Cebpb*$^{-/-}$ AM (right) cytospins. Scale bar = 50µm. All experiments were performed twice with similar results (n=2-4 mice per genotype and experiment; mean ± SD).

1216

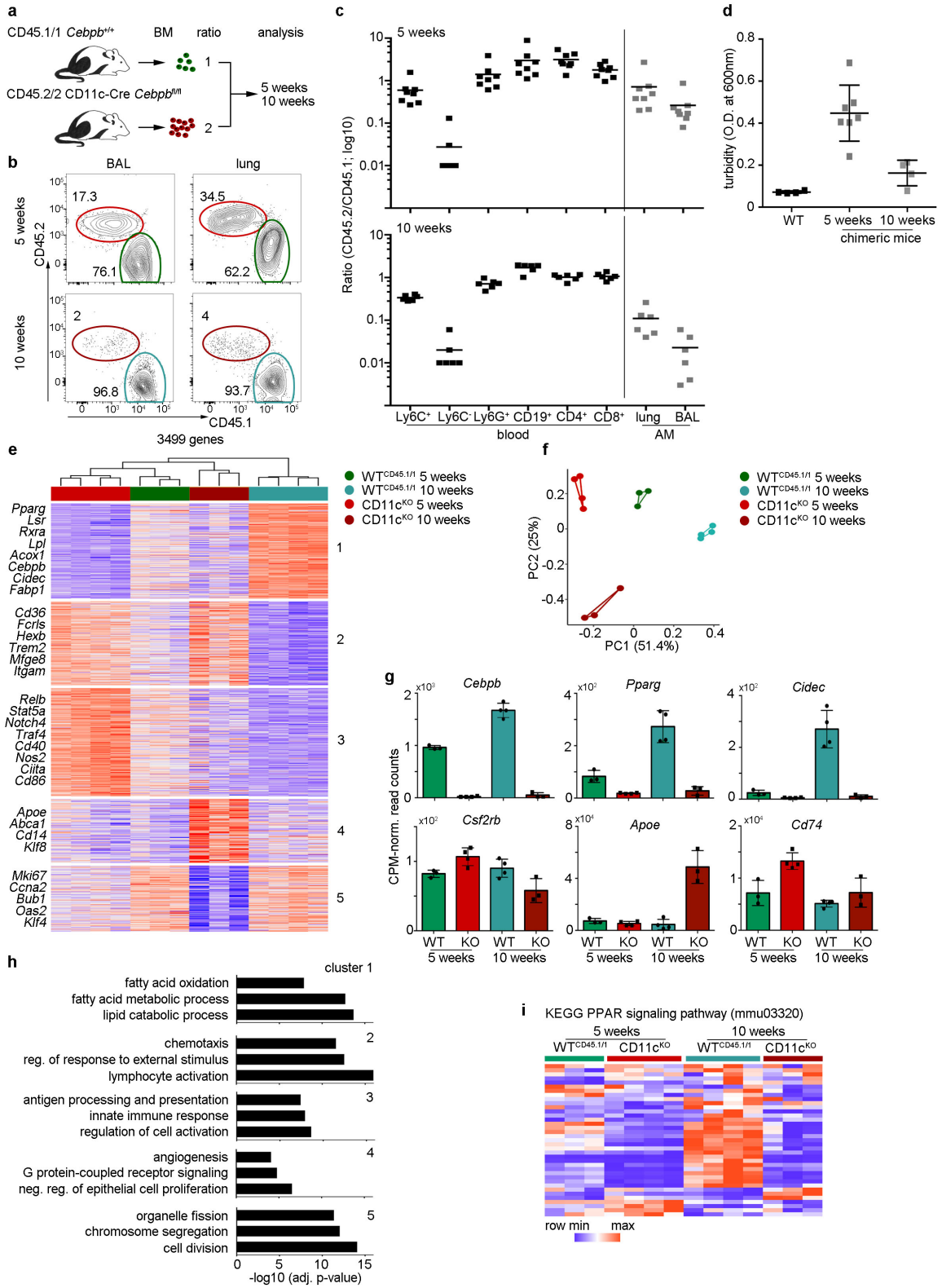

Figure 4

1217
1218 **Figure 4**. C/EBPβ is required for the development of AMs from BM-derived cells after
1219 irradiation.

(A) Schematic representation of bone marrow (BM) transplantation experiment. **(B)** Exemplary flow cytometric analysis of BAL and lung AMs isolated from chimeric mice 5 and 10 weeks after BM transplantation. **(C)** Ratio of CD45.2^{+} CD11c-Cre *Cebpb*$^{fl/fl}$ to CD45.1^{+} WT leukocytes in the blood and lungs of recipient mice 5 weeks (upper panel) and 10 weeks (lower panel) after BM transfer. Shown are pooled data from two independent experiments with each n=3-5 mice per group. **(D)** Turbidity of BAL fluid isolated from mixed BM chimeric mice and WT control animals as measured by the optical density at 600nm. **(E)** CD45.1^{+} WT (WT$^{CD45.1/1}$) and CD45.2^{+} CD11c-Cre *Cebpb*$^{fl/fl}$ (CD11c^{KO}) donor-derived AMs were FACS-purified from the lungs of recipient mice 5 and 10 weeks after BM transplantation and subjected to RNA-seq analysis. 3-4 animals per group were used. Shown are DEGs (adj. p-value < 0.01 and |log2FC| > 1 in at least one pairwise comparison) that were clustered in 5 groups. **(F)** Principal component analysis of the RNA-seq samples described in E. **(G)** Gene expression examples of important AM genes. Shown is the mean ± SD of CPM-normalized read counts. **(H)** Gene ontology enrichment analysis of the heatmap clusters depicted in E. Only biological process terms are shown. **(I)** Expression of genes involved in the KEGG PPAR signaling pathway (mmu03320) in the AM groups described in E. Shown are only genes that were detected with >10 reads in at least one group.

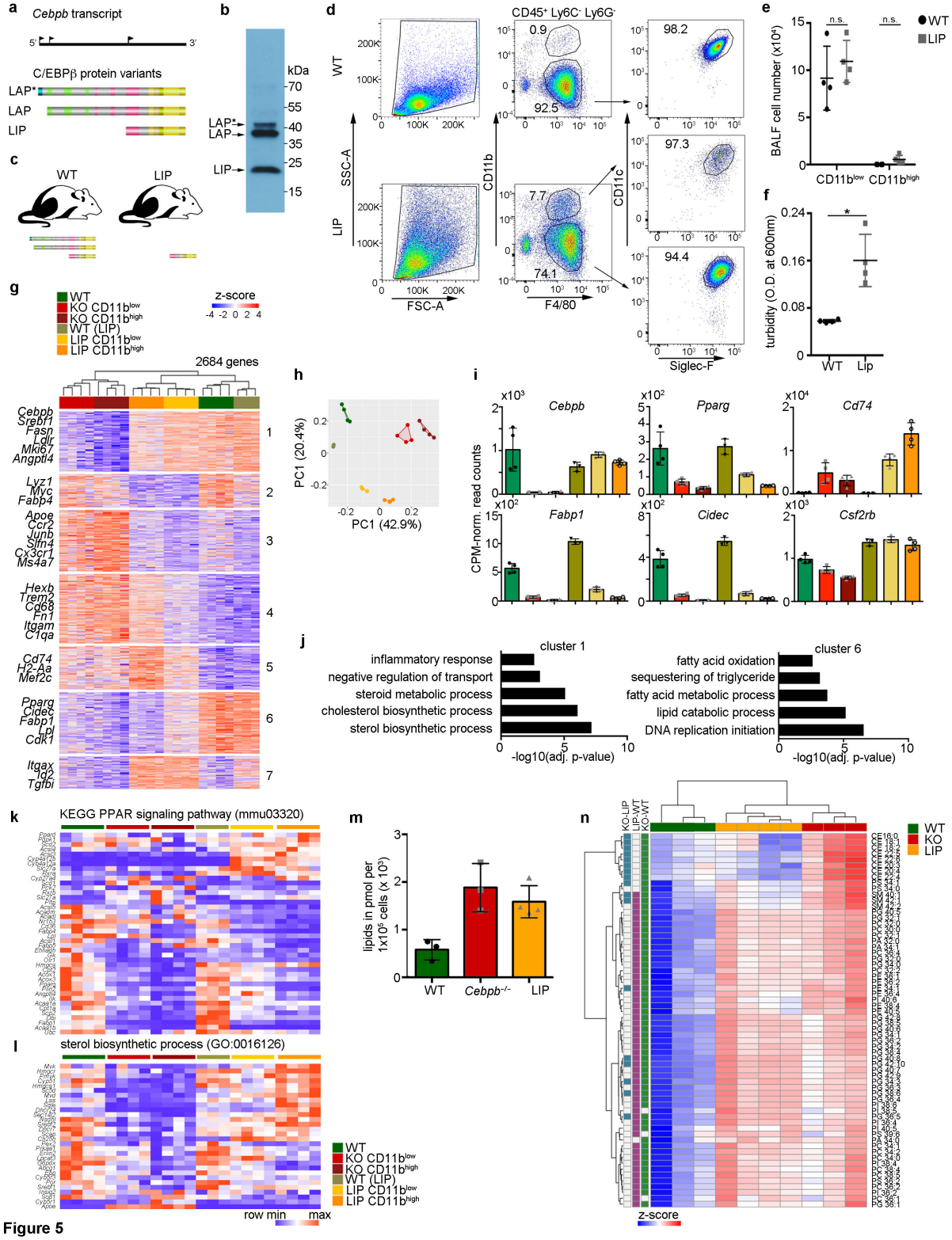

Figure 5

Figure 5. Partial rescue of the C/EBPβ-deficient phenotype by LIP expression.

(A) Depiction of the different translational start sites of the *Cebpb* transcript and the resulting three alternative C/EBPβ protein variants. **(B)** Western blot analysis of C/EBPβ isoform expression in protein extracts of WT AMs from BAL fluid. **(C)** Scheme of LIP mice, which harbor a knockin of the short C/EBPβ LIP isoform at the endogenous *Cebpb* locus. **(D)** Exemplary flow cytometric analysis of AMs isolated by BAL from homozygous LIP knockin

mice (*Cebpb*$^{LIP/LIP}$) and littermate controls. **(E)** Quantification of BAL AM cell numbers in LIP and control mice. **(F)** Turbidity of the BAL fluid isolated from LIP mice and littermate controls as measured by the optical density at 600nm. All experiments depicted in D-F were repeated at least twice (n=4 female mice per genotype and experiment; mean ± SD) with similar results. **(G)** CD11b^{high} (orange) or CD11b^{low} (yellow) LIP and littermate control (olive) AMs were sorted from BAL fluid, analyzed by RNA-seq and compared to *Cebpb*$^{-/-}$ AMs (n=3-4). The heatmap shows DEGs (adj. p-value < 0.01 with a $|log2FC| > 1$ between at least two of the groups). See also Suppl. Data 3 for full description of DEGs in adult LIP AMs. **(H)** Principal component analysis of the RNA-seq results with color code as in G. **(I)** Gene expression examples of important AM genes. The mean ± SD of CPM-normalized read counts is shown. **(J)** Gene ontology enrichment analysis of cluster 1 (specifically downregulated in *Cebpb*$^{-/-}$ AMs) and cluster 6 (commonly downregulated in *Cebpb*$^{-/-}$ and LIP strains) of the heatmap shown in G. Only biological process terms are shown. **(K)** Heatmap showing the expression of genes involved in the KEGG PPAR signaling pathway (mmu03320). Shown are only genes that were detected with >10 reads in at least one group. **(L)** Heatmap showing the expression of genes involved in the GO pathway 'sterol biosynthetic process' (GO:0016126). Shown are only genes that were detected with >20 reads in at least one group. **(M)** Total amounts of membrane and storage lipids in $1x10^5$ FACS-isolated AMs from WT (n=3), *Cebpb*$^{-/-}$ (n=3) and LIP (n=4) mice. **(N)** Analysis of lipid types in AMs from WT (green), *Cebpb*$^{-/-}$ (red) and LIP (yellow) mice. Shown are lipids with p-value ≤ 0.05 as determined by Wilcoxon signed-rank test. The z-score is based on log2 transformed pmol/$1x10^5$ cells values.

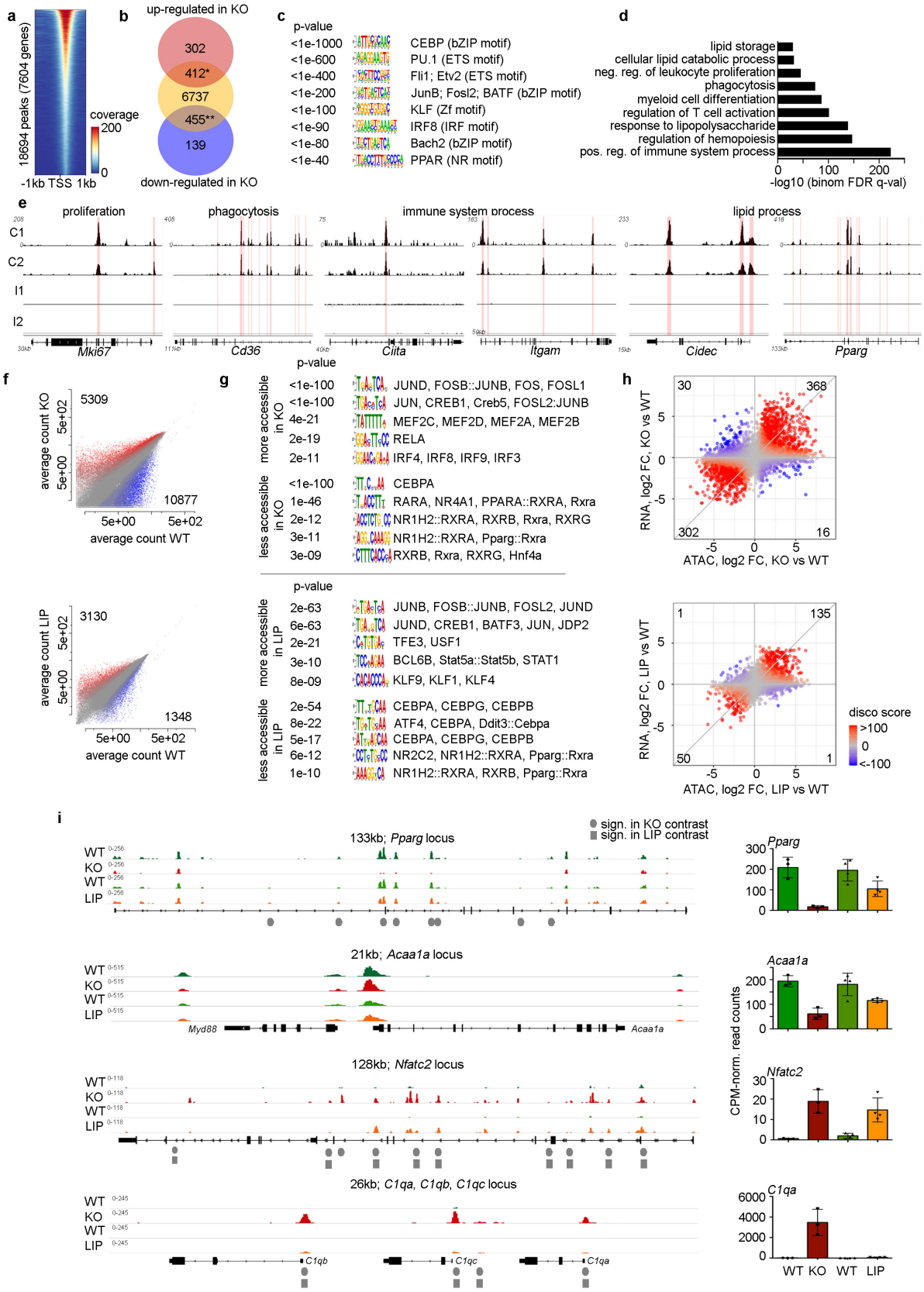

Figure 6

Figure 6. C/EBPβ-dependent epigenetic changes in AMs.

(A) ChIPmentation analysis of the C/EBPβ-DNA binding in BAL-isolated WT AMs was performed in duplicates. Shown are the peak intensities and localization of C/EBPβ binding sites in respect to the closest transcriptional start site (TSS). **(B)** Overlap of the differentially

expressed genes in *Cebpb*$^{-/-}$ AMs shown in Fig. 2D and the C/EBPβ-bound genes found in WT AMs. Significance was tested against a random set of genes with Fisher's exact test. * indicates a p-value of 1.1e-8 and ** p = 2.2e-16. See also Suppl. Data 4 for full description of C/EBPβ-bound regions and overlapping genes. **(C)** Analysis of enriched TF motifs within C/EBPβ binding regions. Results are depicted as motif sequence with corresponding TF annotation and enrichment p-value. **(D)** GO enrichment analysis of the 7604 genes assigned to C/EBPβ binding sites. **(E)** Selected examples of gene loci involved in the indicated biological processes that show significant C/EBPβ binding (red areas) compared to input control. C = ChIP sample; I = Input DNA sample. See also fig. S4A. **(F)** AMs from KO, LIP and littermate controls were isolated by FACS and analyzed by ATAC-seq. Scatter plots showing the chromatin accessibility in the KO contrast (WT vs. KO; upper graph; n=3 mice per genotype) and in the LIP contrast (WT vs. LIP; lower graph; n=4 mice per genotype) depicted as the average read counts of all detected peaks. Colored dots correspond to significantly differential peaks ($q < 0.05$ and $|log2FC| > 2$; red: more accessible in mutant strain; blue: less accessible in mutant strain). **(G)** The differential peaks shown in F were used for motif enrichment analysis. Results are depicted as motif sequence with corresponding TF annotation and enrichment p-value. Upper part: *Cebpb* KO contrast; lower part: LIP contrast. **(H)** "Disco" plots showing the concordance between ATAC-seq and RNA-seq data. ATAC-seq peaks were assigned to genes according to their genomic location and their log2 fold change (FC) between WT and KO (upper graph) and between WT and LIP (lower graph) AMs was ploted against the log2 FC of gene expression of the assigned gene as determined by RNA-seq analysis of the same AM samples. Genes with a high concordance (determined by the disco score) are shown in red and genes with a discordance in blue. For each quadrant the number of concordant or discordant genes with a $|disco\ score| > 100$ is indicated. **(I)** ATAC-seq IGV tracks of representative gene loci with corresponding gene expression (shown as CPM-normalized read counts; mean ± SD) of the same AM samples as determined by RNA-seq. Grey circles indicate significant peak changes ($q < 0.05$ and $|log2FC| > 2$) in the KO contrast, grey squares indicate significant peak changes in the LIP contrast. See also Suppl. Data 5+6 for a full list of accessible regions.

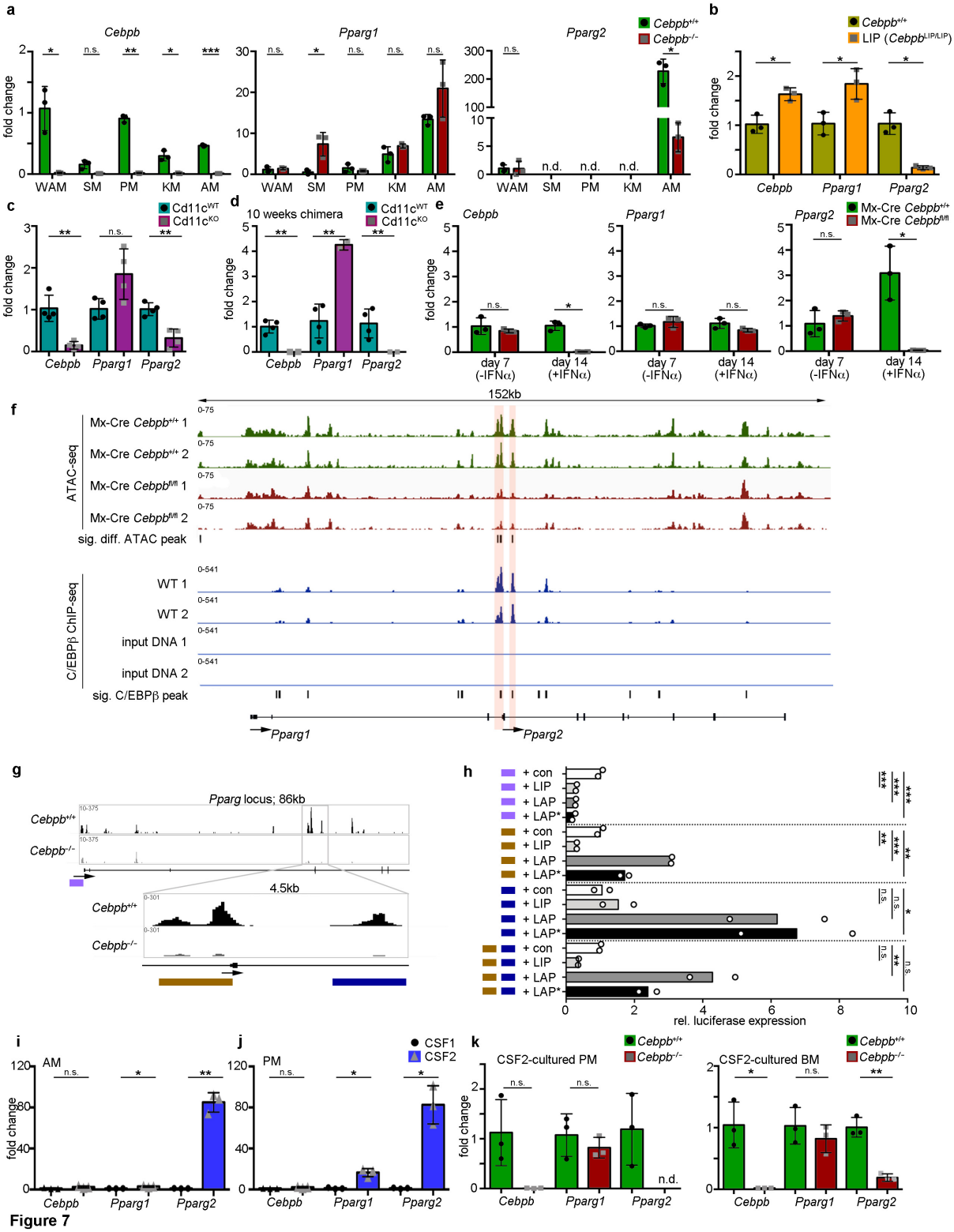

Figure 7

Figure 7. C/EBPβ regulates *Pparg2* expression in AMs

(A) Quantitative real-time PCR (qPCR) of *Cebpb*, *Pparg1* and *Pparg2* mRNA expression in white adipose-tissue macrophages (WAM), spleen macrophages (SM), peritoneal macrophages (PM), kidney macrophages (KM) and AMs isolated by FACS from WT (green) and *Cebpb*-deficient mice (red). n.d. = not detectable. Data is normalized to expression in WT WAM samples. **(B to D)** *Cebpb*, *Pparg1* and *Pparg2* mRNA expression in AMs isolated by FACS from (B) LIP mice (orange) and controls (olive), (C) CD11c-Cre *Cebpb*$^{fl/fl}$ mice

(purple) and controls (turquoise), (D) CD11c-Cre *Cebpb*$^{fl/fl}$ (CD11c^{KO}) and CD11c-Cre *Cebpb*$^{+/+}$ (CD11c^{WT}) AMs isolated from mixed BM chimeras 10 weeks after transfer. Data is normalized to expression in WT samples. **(E)** qPCR of *Cebpb*, *Pparg1* and *Pparg2* expression in AMs isolated from Mx-Cre *Cebpb*$^{fl/fl}$ (red) and Mx-Cre *Cebpb*$^{+/+}$ control mice (green) was performed at day 7 (-IFNα) and at day 14 (+IFNα). For experimental scheme see Fig. 3B. Data is normalized to expression in day 7 (-IFNα) WT samples. **(F)** Upper four IGV tracks: ATAC-seq data derived from day 14 IFNα-treated Mx-Cre *Cebpb*$^{fl/fl}$ (n=3) and control Mx-Cre *Cebpb*$^{+/+}$ AMs (n=2; for experimental scheme see Fig. 3B). Regions with significant changes in accessibility between the genotypes are indicated underneath the tracks. Lower four IGV tracks: C/EBPβ binding as determined by ChIPmentation in WT AMs (n=2). Input samples served as controls. Significant C/EBPβ-bound regions are indicated underneath the tracks. **(G)** Closer representation of ATAC-seq tracks of the *Pparg* locus in WT and *Cebpb*$^{-/-}$ AMs. Indicated are the *Pparg1* promoter (violet), *Pparg2* promoter (brown) and *Pparg2* enhancer (blue) regions used for luciferase reporter constructs. **(H)** *Cebpb* KO MEFs were transfected with *Pparg* promoter/enhancer pGL4.10 constructs (color code as in G) and received either control (con; pcDNA3.1) or *Cebpb* vectors (LAP*, LAP and LIP in pcDNA3.1). Shown is the fold change of luciferase activity to control-treated cells. Mean with n=2. Experiment was repeated twice. **(I** and **J)** *Cebpb*, *Pparg1* and *Pparg2* expression in AMs and PMs cultured with CSF1 or CSF2 for 48h. Data is normalized to expression in CSF1 samples. **(K)** *Cebpb*, *Pparg1* and *Pparg2* expression in PMs cultured with CSF2 for 48h (left panel) and CSF2-cultured BM-derived cells (right panel) isolated from *Cebpb*$^{-/-}$ (red) and control mice (green). Data is normalized to expression in WT samples. Data in A-E and I-K are shown as mean fold change ± SD with n=3-4 mice per genotype.

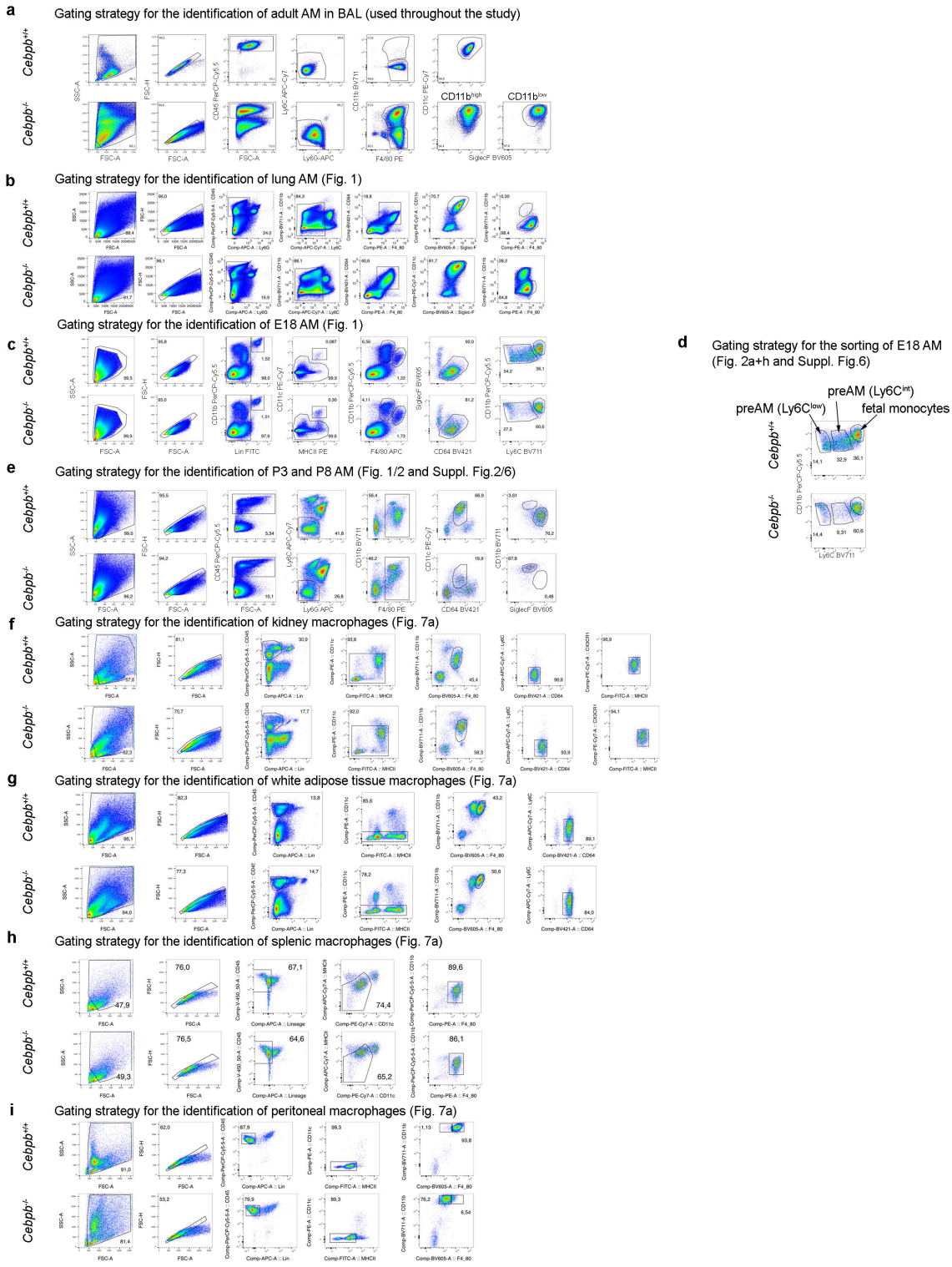

Supplementary Figure 1

Figure S1. Gating strategy for the identification of AMs and other TRMs

(A) Shown is the gating strategy for the identification and sorting of adult AMs from BALF as used throughout the study. **(B)** Gating strategy for adult AMs from lung tissue. **(C)** Gating strategy for the identification of embryonic alveolar macrophage precursor cells (E18). **(D)** Indication of the sorting gates that were used to isolate fetal monocytes, pre-AM I (Ly6Cint) and pre-AM II (Ly6Clow) as shown in Fig. 2A-B and fig. S6. **(E)** Gating strategy for postnatal day 3 and 8 alveolar macrophages from lung tissue. **(F-I)** Gating strategies for the

identification of different tissue-resident macrophages isolated from WT and *Cebpb*$^{-/-}$ mice as used in Fig. 7A. Shown are kidney macrophages (KM) in **(F)**, white adipose-tissue macrophages (WAM) in **(G)**, spleen macrophages (SM) in **(H)** and peritoneal macrophages (PM) in **(I)**.

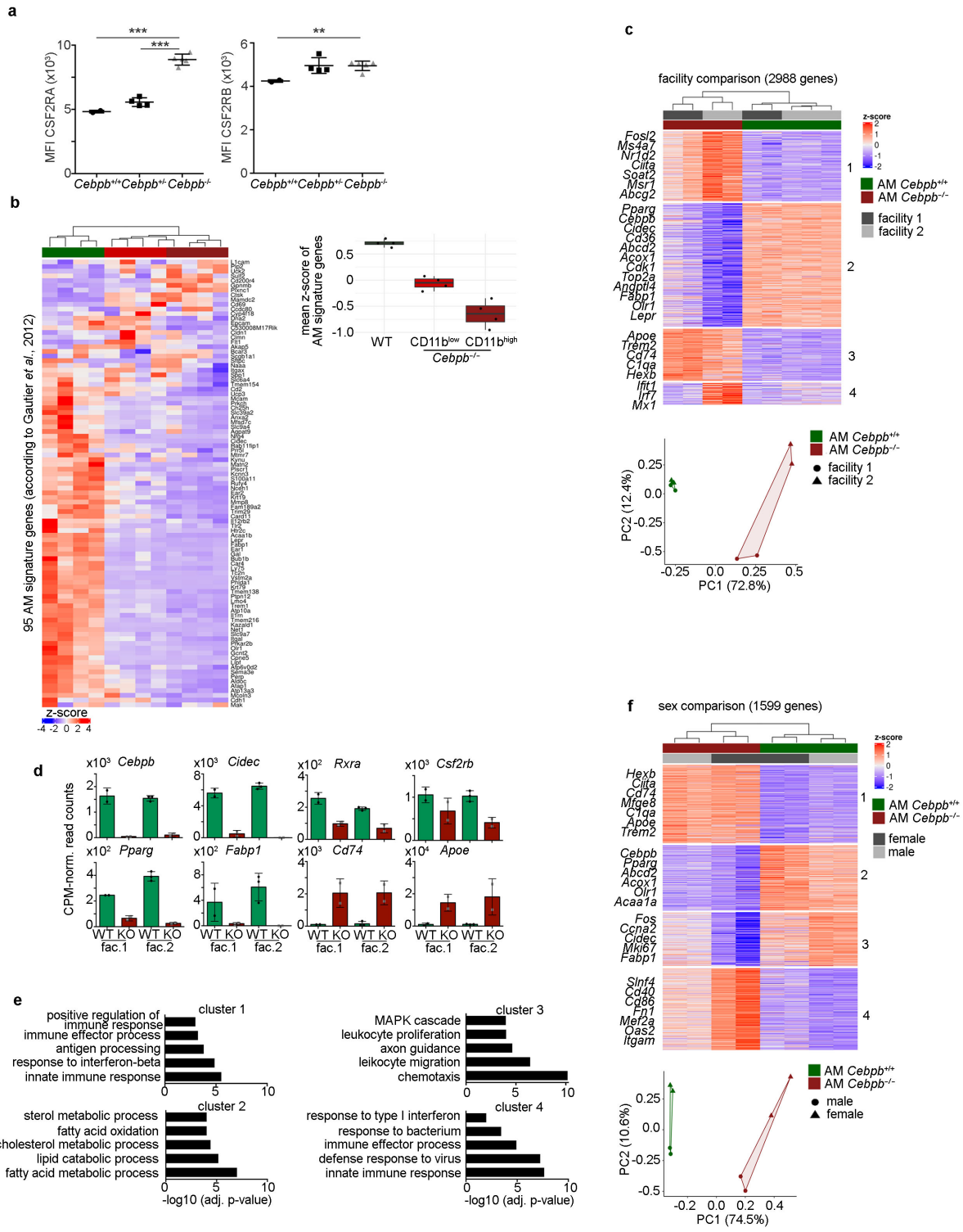

Supplementary Figure 2

Figure S2. Influence of housing condition and sex on the transcriptome of *Cebpb*-deficient AMs.

(A) Shown are the median fluorescence intensities (MFI) of CSF2RA (left panel) and CSF2RB (right panel) levels in P8 AMs isolated from *Cebpb*$^{+/+}$, *Cebpb*$^{+/-}$ and *Cebpb*$^{-/-}$ animals. **(B)** Heatmap (left panel) and average z-score (right panel) presenting the expression of 95 AM signature genes (*13*) that could be detected in *Cebpb*-deficient AMs and controls. **(C)** Heatmap depicting the transcriptomic differences between WT and *Cebpb*$^{-/-}$ AMs from two

different mouse facilities. CD11b^{low} and CD11b^{high} AMs from KO animals were pooled for this analysis. Shown are genes with adj. p-value < 0.01 and |log2FC| > 1 in at least one pairwise comparison. Cluster 1 consists of 780 genes, cluster 2 of 1381 genes, cluster 3 of 582 genes and cluster 4 of 245 genes. Note that lipid metabolism-related genes like *Pparg*, *Cidec*, *Fabp1* and *Cd36* are part of cluster 2 and downregulated in KO AMs independent of the facility. PC analysis indicates the similarity between the groups. Component 1 (*Cebpb* gene deficiency) and not component 2 (facility) explains most of the gene expression changes. **(D)** Gene expression examples of AM genes of interest. The mean ± SD of CPM-normalized read counts is shown. **(E)** GO enrichment analysis of the 4 clusters depicted in c. Cluster 2 is enriched for lipid processing. **(F)** Heatmap depicting the transcriptomic changes between male and female WT and pooled CD11b^{high} and CD11b^{low} *Cebpb*$^{-/-}$ AMs. Shown are genes with adj. p-value < 0.01 and |log2FC| > 1 in at least one pairwise comparison. Cluster 1 consists of 448 genes, cluster 2 of 374 genes, cluster 3 of 309 genes and cluster 4 of 468 genes. PCA analysis indicates the concordance between the groups. Component 1 (*Cebpb* gene deficiency) and not component 2 (sex) explains most of the gene changes. N=2-3 animals per genotype and condition.

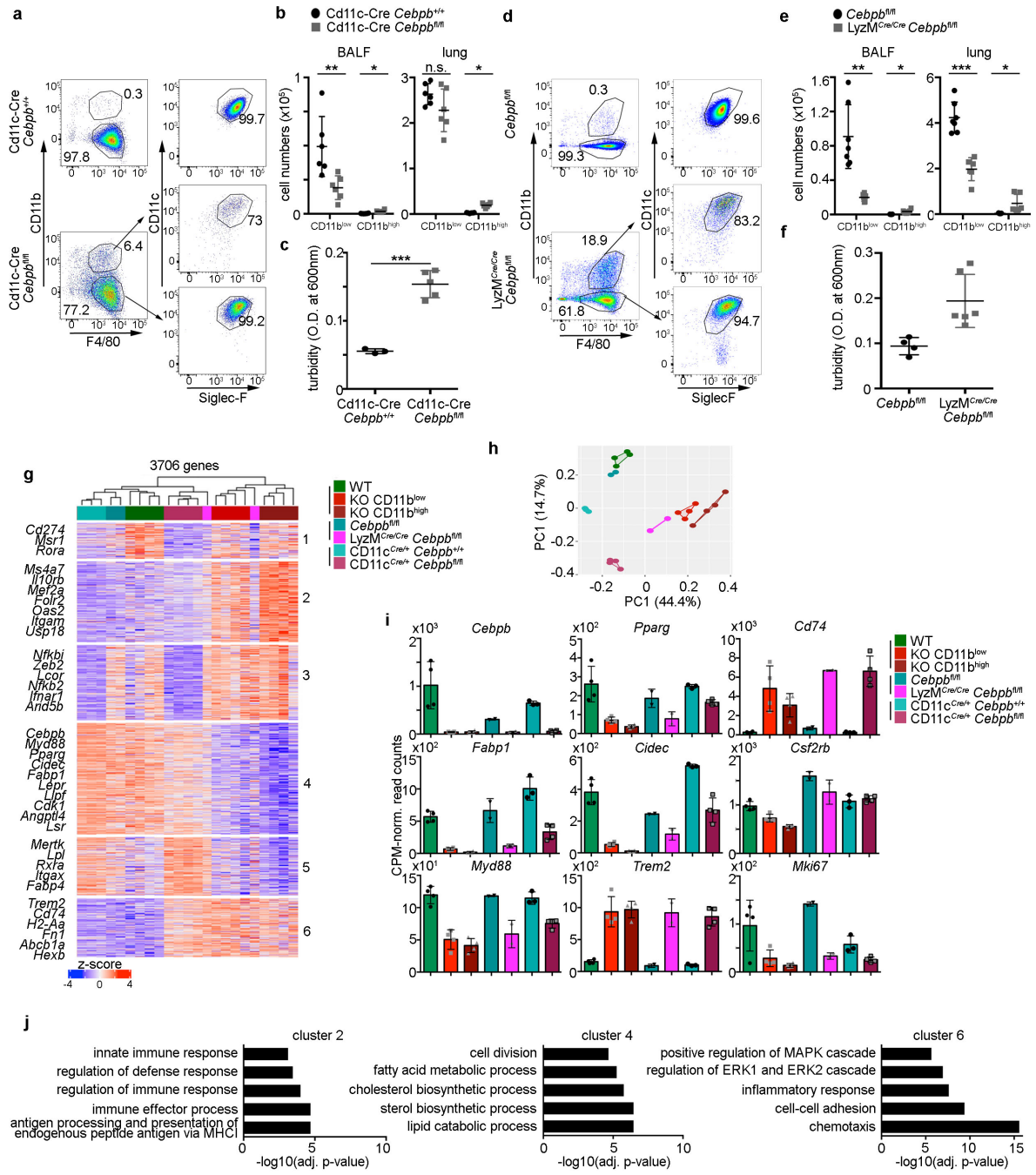

Supplementary Figure 3

Figure S3. Analysis of AMs from conditional *Cebpb*-deficient mice.

(A) Representative flow cytometric analysis of BALF isolated from CD11c-Cre *Cebpb*$^{+/+}$ and CD11c-Cre *Cebpb*$^{fl/fl}$ animals. **(B)** Quantification of CD11b^{low} and CD11b^{high} total AM cell numbers in CD11c-Cre *Cebpb*$^{+/+}$ and CD11c-Cre *Cebpb*$^{fl/fl}$ animals. **(C)** Turbidity measurement of BALF isolated from CD11c-Cre *Cebpb*$^{+/+}$ and CD11c-Cre *Cebpb*$^{fl/fl}$ animals at OD600nm. **(D)** Exemplary flow cytometric analysis of BALF isolated from *Cebpb*$^{fl/fl}$ and LyzM$^{Cre/Cre}$ *Cebpb*$^{fl/fl}$ animals. **(E)** Quantification of CD11b^{low} and CD11b^{high} total AM cell numbers in *Cebpb*$^{fl/fl}$ and LyzM$^{Cre/Cre}$ *Cebpb*$^{fl/fl}$ animals. **(F)** Turbidity measurement at OD600nm of BALF isolated from *Cebpb*$^{fl/fl}$ and LysM$^{Cre/Cre}$ *Cebpb*$^{fl/fl}$ animals. **(G)** Heatmap

depicting the transcriptomic differences between the indicated genotypes. Shown are genes with adj. p-value < 0.01 and |log2FC| > 1 in at least one pairwise comparison. **(H)** PC analysis indicates the similarity between the genotypes. Color code as in g. **(I)** AM gene expression examples. The mean ± SD of CPM-normalized read counts is shown. **(J)** GO enrichment analysis of the clusters depicted in g. No significant GO enrichment was detected for genes in clusters 1, 3 and 5. Note that *Cebpb*$^{-/-}$ (mixed genetic background), LyzM-Cre (C57BL/6 background) and CD11c-Cre (C57BL/6 background) mice were from different facilities. Experiments were performed with 2-6 mice per genotype and show the mean ± SD.

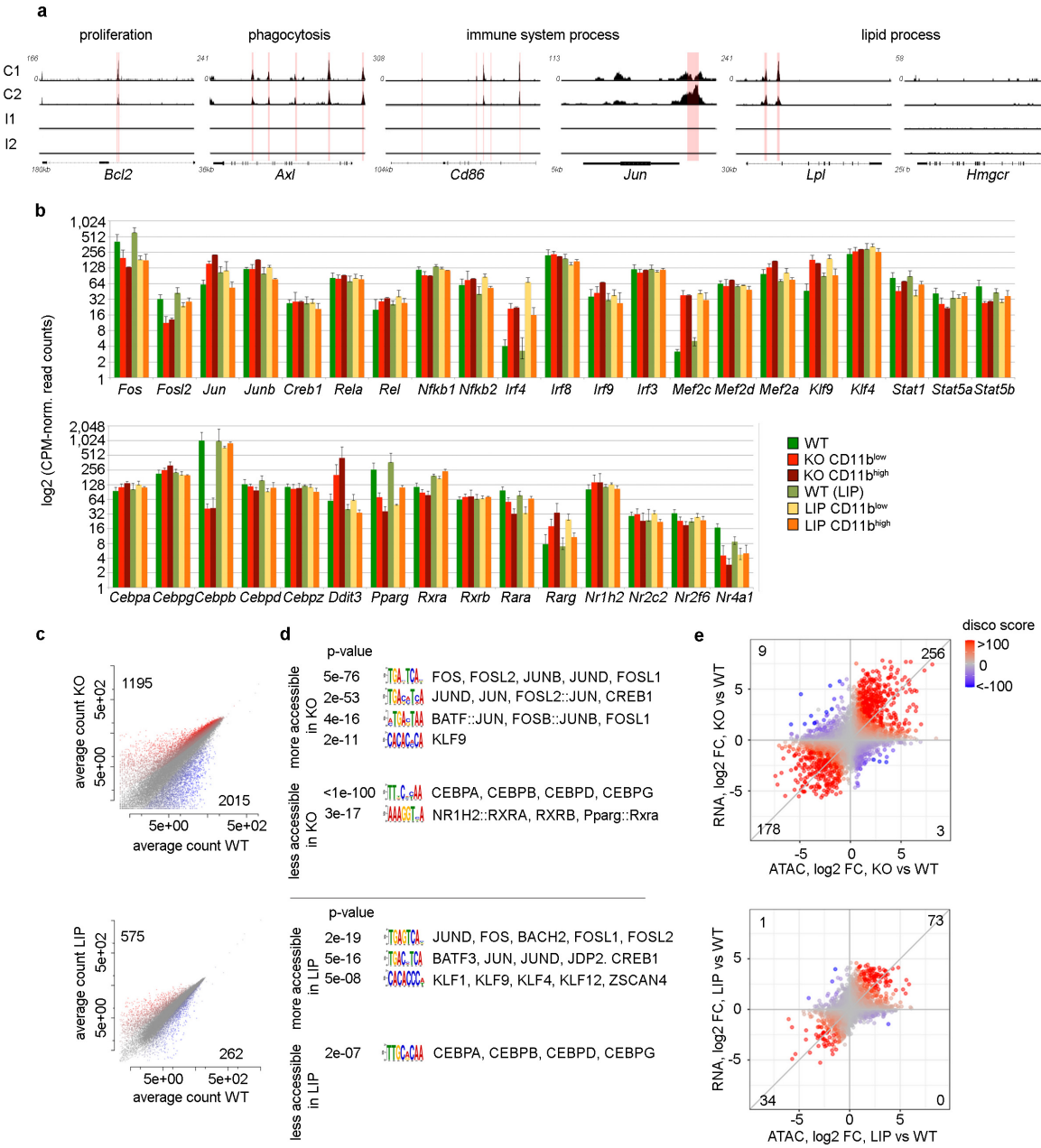

Supplementary Figure 4

Figure S4. Chromatin accessibility in the promoter regions of *Cebpb*$^{-/-}$ and LIP AMs

(A) Additional IGV tracks for genes that show C/EBPb binding. C = ChIP sample; I = Input DNA sample. **(B)** Gene expression of TFs in KO and LIP AMs whose DNA binding motifs were identified by motif enrichment analysis in Fig. 6G. Normalized CPM-read counts ± SD are shown. Note that recent studies have described a compensatory function of the different C/EBP TF family members in several biological settings. We did not detect a compensatory increase of any of the detected C/EBP family members. **(C)** Scatter plots showing the chromatin accessibility (depicted as ATAC-seq peaks) specifically in promoter regions (±3kb TSS) in the KO contrast (WT vs. KO; upper graph; n=3 mice per genotype) and in the LIP contrast (WT vs. LIP; lower graph; n=4 per genotype). Colored dots correspond to peaks which show a significant difference between two conditions compared at q < 0.05 and

1405 |log2FC| > 2. **(D)** The identified differential promoter peaks depicted in b were used for motif
1406 enrichment analysis. Shown are the p-value of enrichment, motif sequence and the
1407 corresponding transcription factor annotation. Upper part: *Cebpb* KO comparison; lower part:
1408 LIP comparison. **(E)** “Disco” plots showing concordance between promoter peak-derived log_2
1409 fold changes and p-values and transcript-derived log_2 fold changes and p-values.
1410
1411

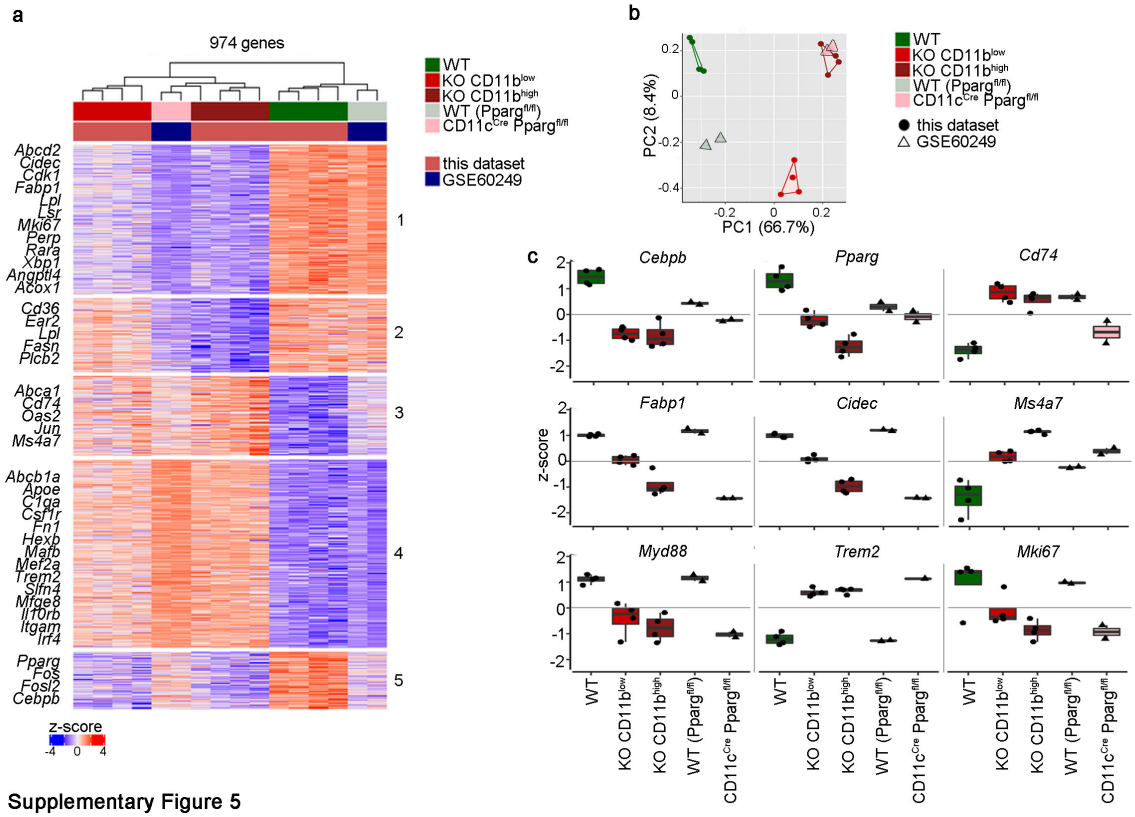

Supplementary Figure 5

Figure S5. Comparison of *Cebpb*$^{-/-}$ AMs and *Pparg*-deficient AMs

(A) Comparison of published microarray data (GSE60249) from *Pparg*-deficient AMs with RNA-seq data of *Cebpb*$^{-/-}$ AMs. Shown are genes with an adj. p-value < 0.01 and $|\log2FC| >$ 1 in at least one of the contrasts: CD11c Cre *Pparg*$^{fl/fl}$ vs. WT (*Pparg*$^{fl/fl}$), KO CD11b^{low} vs. WT and KO CD11b^{high} vs. WT. **(B)** Combined principal component analysis of the two data sets. **(C)** Gene expression examples in the different genotypes. Shown is the mean z-score ± SD.

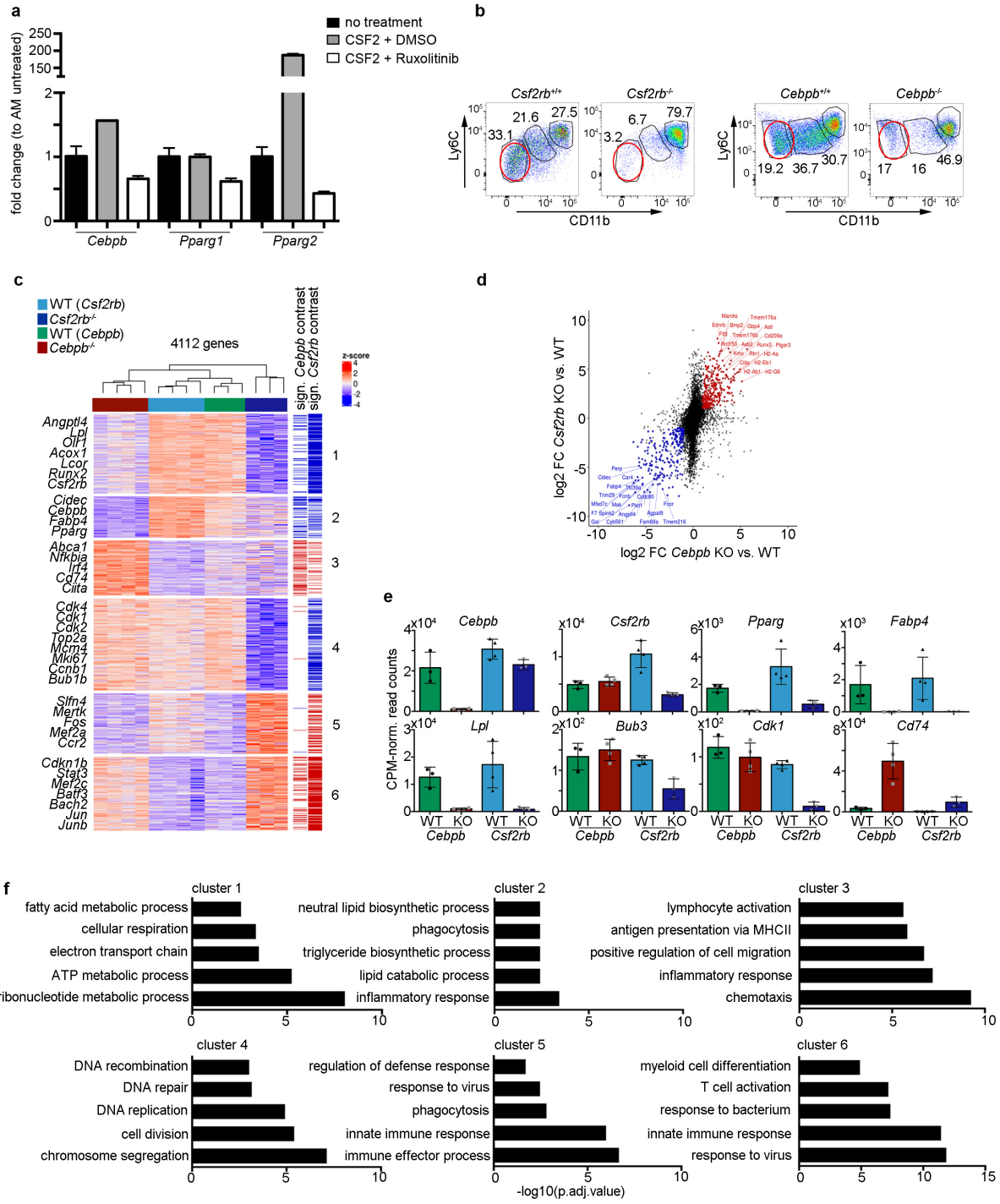

Supplementary Figure 6

Figure S6. *Cebpb* expression is unaffected in Csf2rb-deficient pre-AMs.

(A) qPCR of *Cebpb*, *Pparg1* and *Pparg2* expression in WT AMs cultured without CSF2, with CSF2 and DMSO or with CSF2 and Ruxolitinib for 48h. Data is normalized to expression in untreated samples. **(B)** Representative flow cytometry analysis of pre-AMs isolated from *Csf2rb*$^{-/-}$ (left panel) and *Cebpb*$^{-/-}$ (right panel) animals and respective controls. Ly6C^{low} pre-AMs from *Csf2rb*$^{-/-}$ and *Cebpb*$^{-/-}$ animals were FACS-purified and used for bulk RNA-seq analysis. **(C)** Heatmap depicting the transcriptomic differences between the indicated genotypes. Shown are 4112 genes with adj. p-value < 0.01 and |log2FC| > 1 in at least one

pairwise comparison that could be assigned to 6 cluster. Clusters 4 and 5 were specific to *Csf2rb*$^{-/-}$ cells, while clusters 2, 6 and partially 1 were shared by *Csf2rb*$^{-/-}$ and *Cebpb*$^{-/-}$ pre-AMs. The columns on the right hand of the heatmap indicate significantly differential genes in the *Cebpb* KO contrast (left column) and in the *Csf2rb* KO contrast (right column). Upregulated genes in either KO are marked in red, downregulated genes are marked in blue. **(D)** Scatter plot showing the log2 fold changes of *Cebpb* KO vs. WT gene expression in comparison to expression differences in *Csf2rb* KO vs. WT. Common significant ($p < 0.01$) gene changes are indicated in red (log2FC > 1) or blue (log2FC < -1). **(E)** Gene expression examples of AM genes of interest. The mean ± SD of CPM-normalized read counts is shown. **(F)** GO enrichment analysis of the clusters depicted in b. This analysis indicates that innate immune response-related genes are equally upregulated (*Jun*, *Stat3* and *Junb*), while genes involved in lipid processes (like *Cidec*, *Fabp4*, *Olr1*, and *Angptl4*) are commonly downregulated. Note that *Cebpb*$^{-/-}$ animals are bred on a mixed genetic background whereas *Csf2rb*$^{-/-}$ mice are on C57BL/6 background, which might contribute to differences reflected in cluster 5. 3-4 mice were analyzed per genotype.

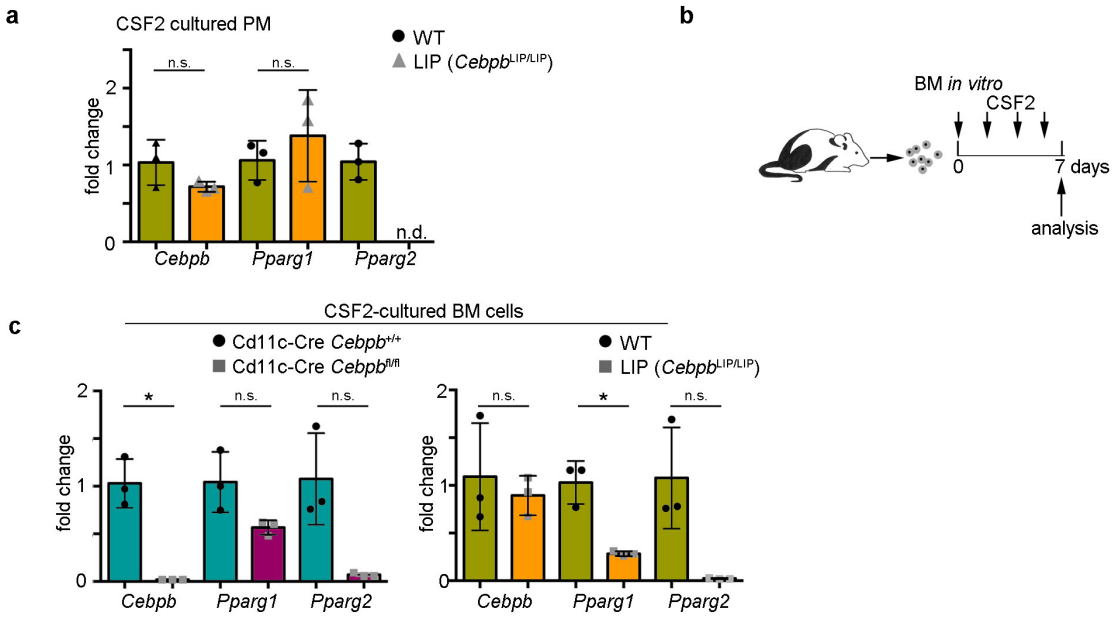

Supplementary Figure 7

Figure S7. CSF2 and C/EBPβ are necessary co-factors for the induction of *Pparg2* in other macrophage subsets.

(A) qPCR analysis of PMs isolated by FACS from LIP (*Cebpb*$^{LIP/LIP}$; orange) and control (olive) animals. The cells were cultured with CSF2 for 48h and *Cebpb*, *Pparg1* and *Pparg2* expression were measured. Data were normalized to the expression in WT cells. Each dot represents one animal and the experiment was repeated twice with similar results. **(B)** Schematic representation of BM culture experiments. BM cells were isolated and cultured with CSF2 for 7 days. Medium and CSF2 was exchanged every second day (left scheme). **(C)** Expression of *Cebpb*, *Pparg1* and *Pparg2* in BM-derived myeloid cells isolated from CD11c-Cre *Cebpb*$^{fl/fl}$ (left graph; purple) and LIP animals (*Cebpb*$^{LIP/LIP}$; right graph; orange) with respective controls (turquoise and olive). Each dot represents one animal and the experiment was repeated twice with similar results. All plots in A-C show the mean fold change ± SD.

Supplementary data 1: Related to Fig. 2. RNA-sequencing results of fetal monocytes, pre-AMs and adult AMs isolated by FACS from *Cebpb*-deficient mice and controls. Represented are the fold changes and p-values of significantly differentially expressed genes in the fetal monocyte and pre-AM contrast (related to Fig. 2A-B; Tab1 and Tab2). CPM-normalized read counts of genes that belong to the heatmap of adult AMs depicted in Fig. 2D are presented in Tab3. Cluster affiliation and significance is indicated.

Supplementary data 2: Related to fig. S3. RNA-sequencing results of *Cebpb*-deficient AMs isolated from constitutive KO animals (*Cebpb*$^{-/-}$) or different conditional Cre mice (CD11c-Cre *Cebpb*$^{fl/fl}$ or LyzM-Cre *Cebpb*$^{fl/fl}$). Shown are the CPM-normalized read counts of the heatmap data depicted in fig. S3G. Cluster affiliation and significance is indicated.

Supplementary data 3: Related to Fig. 5. RNA-sequencing results of AMs isolated from *Cebpb*$^{-/-}$, LIP (*Cebpb*$^{LIP/LIP}$) mice and respective controls. Shown are the CPM-normalized read counts of the heatmap data depicted in Fig. 5G. Cluster affiliation and significance is indicated.

Supplementary data 4: Related to Fig. 6. Depicted in Tab1 are all detected binding regions of C/EBPβ as determined by ChIPmentation. In Tab2 we provide a list of genes that show C/EBPβ binding and are significantly differentially expressed in our transcriptome data (Fig. 2B)

Supplementary data 5: Related to Fig. 6. ATAC-sequencing results of AMs isolated from *Cebpb*$^{-/-}$ mice and respective controls. Shown are all detected peaks, fold change between WT and KO condition and p-values. The results are based on triplicate analysis of each genotype.

Supplementary data 6: Related to Fig. 6. ATAC-sequencing results of AMs isolated from *Cebpb*$^{LIP/LIP}$ mice and respective controls. Shown are all detected peaks, fold change between WT and LIP condition and p-values. The results are based on the analysis of 4 animals per group.

Supplementary data 7: Related to fig. S6. Transcriptome comparison of *Csf2rb*-deficient pre-AMs against *Cebpb*$^{-/-}$ pre-AMs with respective controls. Shown are the CPM-normalized read counts of the heatmap data depicted in fig. S6C. Cluster affiliation and significance is indicated.